J. Phys.: Condens. Matter **24** (2012) 245101 (15pp) doi:10.1088/0953-8984/24/24/245101

Simultaneous measurement of rotational and translational diffusion of anisotropic colloids with a new integrated setup for fluorescence recovery after photobleaching

B W M Kuipers, M C A van de Ven, R J Baars and A P Philipse

Van't Hoff Laboratory for Physical and Colloid Chemistry, Debye Institute for Nanomaterials Science, Utrecht University, Padualaan 8, 3584 CH Utrecht, The Netherlands

E-mail: b.w.m.kuipers@uu.nl

Received 20 February 2012, in final form 10 April 2012
Published 8 May 2012
Online at stacks.iop.org/JPhysCM/24/245101

Abstract

This paper describes an integrated setup for fluorescence recovery after photobleaching (FRAP) for determining translational and rotational Brownian diffusion simultaneously, ensuring that these two quantities are measured under exactly the same conditions and at the same time in dynamic experiments. The setup is based on translational-FRAP with a fringe pattern of light for both the bleaching and monitoring of fluorescently labeled particles, and rotational-FRAP, which uses the polarization of a short bleach light pulse to create a polarization anisotropy. The fringe pattern of the probe beam is modulated in conjunction with a synchronized lock-in amplifier giving a fast, sensitive, ensemble-averaged measurement compared to microscope-image based techniques. The experimental polarization geometry we used ensures that the fluorescence emission is collected without polarization bias. Therefore, only the orientation of the absorption dipole moment of the fixed dye in the particles is measured, which simplifies interpretation of the data. The polarization is modulated rapidly between two orthogonal polarization states, giving the polarization anisotropy in one, single measurement.

The rotational and translational Brownian diffusion of anisotropic colloids is measured for ellipsoids of revolution. This experiment shows that in this case the rotational correlation function matches a three-exponential decay in accordance with theoretical predictions.

S Online supplementary data available from stacks.iop.org/JPhysCM/24/245101/mmedia

(Some figures may appear in colour only in the online journal)

1. Introduction

Experimental studies of translational diffusion with fluorescence recovery after photobleaching (FRAP) [1] have been used frequently to measure the mobility of macromolecules, including proteins and lipids in biological membranes [2], molecules in cytoplasm of living cells [3], micelles [4], synthetic polymers [5], and colloidal particles [6].

The translational part of the integrated FRAP setup with a modulating fringe pattern we employ is essentially the sensitive method developed by Davoust *et al* [7] which was later improved by Imhof *et al* [1] in our group.

Probing of rotational diffusion by FRAP has evolved in the last decade to a sensitive method for measuring the rotational dynamics of fluorescently labeled colloidal particles over a wide dynamic range [8]. By a relatively easy incorporation of dye in the particles, colloids carry

a tag permitting monitoring of their orientation. The accessible time scale for reorientation ranges from tens of microseconds to seconds or more, in contrast to time-resolved phosphorescence anisotropy (TPA) where the maximum reorientation time scale is limited to at most a few milliseconds owing to the finite lifetime of the excited triplet state of the dyes [9–11].

Rotational- and translational-FRAP does not require nearly transparent, optically matched samples as needed in dynamic light scattering (DLS) [12]. Slow diffusion processes can be investigated due to the irreversibility of the photobleaching reaction. Unlike birefringence measurements, the measured quantity in rotational-FRAP is not proportional to the concentration of the particles.

Here we present the development of an integrated translational and rotational setup. The simultaneous measurement of translational and rotational motion clearly is an advantage for a number of situations. The integrated setup ensures that translational and rotational diffusion coefficients are measured under exactly the same conditions, and simultaneously in dynamic experiments, e.g. in a sedimenting–diffusion profile. In addition, coupling of rotational and translational motion, manifested by a non-diagonal diffusion tensor, can be investigated. Another example is the situation in which one of both diffusional motions is hindered, e.g. in a rotator phase [13]. As a useful application, the absolute length of the long and short axis of a colloidal ellipsoid of revolution (spheroid) can both be measured in one single experiment. This also applies to spheroids with a small aspect ratio. Their dimensions are difficult to derive from rotational-FRAP only [14]. In the integrated translational–rotational method described here, two independent correlation functions, one for translational as well as one for rotational diffusion, are obtained for each coordinate in reciprocal space. This is in contrast with the case of depolarized dynamic light scattering (DDLS) [12] where only one correlation function is measured comprising both a weighted translational and rotational part. Likewise, in fluorescence correlation spectroscopy (FCS) [15, 16] only one correlation function is obtained when translational and rotational diffusion are measured simultaneously.

The development of our integrated technique starts from the setup designed by Tinland *et al* [17]. We improved the setup by implementing the experimental configuration of the rotational setup employed by Lettinga and Koenderink [8] in our group, with the difference that we use a fast photoelastic modulator (PEM) to modulate the polarization: the mechanical rotating polarizer from [8] would distort the fringe pattern in translational-FRAP. Our specific experimental polarization geometry ensures that only the absorption dipole moment in the rotational correlation function is measured, simplifying interpretation of the data [18] compared to the setup of Tinland [17] and the optical microscopy geometries used elsewhere [19]. In the latter geometries, the polarization of fluorescence detection is biased with the disadvantage that also the emission dipole orientation is measured, giving a higher-order rotational relaxation contribution to the polarization anisotropy that decays at a faster rate. Use of a short intense bleach laser pulse in combination with a fast ferroelectric liquid crystal shutter [8] in front of the fluorescent light detector gives access to reorientation correlation times down to sub-milliseconds.

Section 2.1 describes the principle of FRAP in general and section 2.2 describes translational-FRAP specifically. Section 2.3 presents the principle of rotational-FRAP. Section 3 reviews the theory of the rotational and translational dynamics of an ellipsoid of revolution. The experimental setup is described in section 4, with an overview of the measures taken to make the combination of translational and rotational-FRAP feasible. The performance of the new integrated translational–rotational-FRAP setup is demonstrated in section 5 and measurements on ellipsoids of revolution are presented as a proof of principle for the application of our setup to anisotropic particles.

2. The integrated FRAP method

2.1. Principle

FRAP is a so-called pump-and-probe technique. Initially, a high-intensity light pulse illuminates a spot or pattern inside the sample. In this way, a photochemical process called photobleaching irreversibly destroys the fluorescence of dye inside the particles in part of the sample. After this pump pulse the return of the fluorescence from the bleached part of the sample due to diffusion is monitored in time by a probe beam, which has a low intensity so that subsequent bleaching is insignificant. The bleach pattern gradually fades away by exchange translational diffusion.

Brownian motion not only comprises translational but also rotational diffusion. This rotational motion consists of small angular steps in random directions. In rotational or polarized FRAP, the polarization property of the light is used to keep track of this rotational motion [8]. Dyes rigidly incorporated in the particles are bleached preferentially when they have the orientation of their absorption dipole moment parallel to the polarization direction of the pump beam. This creates an anisotropic distribution of bleached dye molecules, and hence induces polarization anisotropy called linear dichroism due to absorption anisotropy. This can be probed by the fluorescence intensity of the ensemble of particles in the bleached region by modulation of the polarization direction of a probe beam. Little dye will be excited when the polarization direction of the probe beam is parallel to that of the bleach beam, since a large number of dye molecules with this absorption transition dipole moment orientation have been bleached. Consequently, there will be less emission of fluorescent light. On the other hand, if the polarization direction is perpendicular to that of the bleach beam, the excitation probability is high due to the high absorption of light. Since the dyes with their absorption dipole moment in this direction have hardly been bleached, there will be a high emission of fluorescent light. This polarization anisotropy is large shortly after the bleach pulse but gradually fades away by the rotational Brownian motion.

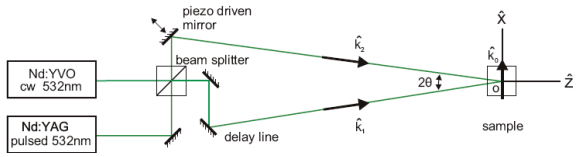

Figure 1. Schematic diagram of the translational part of the integrated rotational- and translational-FRAP setup with the wavevectors $\hat{\mathbf{k}}_i$. The origin of the left-handed Cartesian coordinate system is on the point of intersection of the crossed beams in the middle of the sample.

2.2. Translational-FRAP

In the translational part of our FRAP setup, the intensity distribution of the bleach pattern in the sample is a sinusoidal fringe obtained by the interference of two intersecting beams, derived by splitting the original beam in two equal parts with a beam splitter and recombining them under a semiangle θ with the help of mirrors (see figure 1). The probe fringe is generated in the same way, but with a low-intensity continuous wave laser beam with the same wavelength λ.

After the bleach pulse, the concentration of particles with photobleached dye has an approximately sinusoidal profile. It has to be emphasized that after the bleach pulse the distribution of bleached and unbleached dye is changed but the concentration of colloidal particles remains homogeneous. The process of the fade away of this bleach pattern by exchange translational diffusion of the particles obeys a special case of the Smoluchowski equation [12], which has the following solution, after Fourier transformation to the reciprocal space,

$$P(\mathbf{q}|t) = (2\pi)^{-1} \mathrm{e}^{-D^{\mathrm{t}} q^2 t}. \tag{1}$$

This can be recognized as the self-intermediate scattering function, with D^{t} the long time self-diffusion coefficient; t is the time and q the length of the wavevector (see [1]).

After the bleach pulse, the spatial phase offset ('x' position in figure 1) of the sinusoidal profile is adjusted by a piezo-driven mirror (see figure 1) such that the maxima of the probe fringe is coincident with the minima in the concentration profile of the unbleached dye. Then the exponential rise of the fluorescence intensity due to exchange diffusion of bleach and unbleached particles is maximal. The optimum choice of this spatial phase offset when modulation of the probe fringe pattern is applied will be treated in section 4.

The piezo-driven mirror is also used for the modulation of the probe fringe. The spatial phase $\varphi(t')$ is time (t') dependent due to the optical path difference $\Delta\Lambda_{\mathrm{opd}}$ caused by the sinusoidal movement of this mirror. This results in a probe fringe pattern which slides periodically in the x-direction over the bleached dye concentration profile. It can be shown [1] that the fringe spacing equals $L = \lambda/2 \sin\theta$ with λ the wavelength of the light in vacuum and a reciprocal spacing $k_0 = 2\pi/L$ in the direction perpendicular to the bisector of the intersecting beams.

An approximation for the fluorescence intensity is derived by Imhof and Dhont [20] for the case of a number of fringe lines N_{lines} in the bleach pattern of more than 30:

$$I_{\mathrm{f}}(t, t') \propto A(t) Q I_{\mathrm{p}}^0 N_{\mathrm{p}} n_0 \{I_{\mathrm{dc}}^*(K, N_{\mathrm{lines}}) + I_{\mathrm{mod}}^*(K, N_{\mathrm{lines}}) \times \cos[\varphi(t')] \mathrm{e}^{-D^{\mathrm{t}} k_0^2 t}\} \tag{2}$$

with N_{p} the number of identical Brownian particles in the volume V that is illuminated, and n_0 the average of the pre-bleach number of dye molecules in a particle. Not all bleached dye is bleached in an irreversible way, therefore $A(t)$ accounts for the return of the remaining reversible bleached molecules to the ground state. The constant Q is a product of the dye quantum efficiencies for photon absorption and emission on the one hand, and the detection efficiency on the other hand. $K = \alpha I_b^0 \Delta t_b$ is the mean bleaching efficiency index, which is a measure for the bleach depth and α is the photolytic constant that relates to the efficiency of the bleaching process. I_b^0 and I_{p}^0 are the bleach and probe intensities, respectively, and Δt_b the bleach pulse duration. The fluorescence intensity in equation (2) consists of two parts: a constant background fluorescence with magnitude I_{dc}^*. This term is a generalization of the modified Bessel function and depends on the bleach depth K and number of fringes N_{lines}. The second term with amplitude I_{mod}^* is the modulated part, which falls off almost single exponentially for a number of fringes N_{lines} above 30. The latter condition is necessary to neglect the translational diffusion of particles to and from the exterior of the fringe area.

2.3. Rotational-FRAP

If a unit director $\hat{\mathbf{D}}$ is assigned to a spherical Brownian particle, the endpoint of $\hat{\mathbf{D}}$ describes small random angular steps on the surface of a hypothetical unit sphere due to the collision with solvent molecules. The probability $P(\hat{\mathbf{D}}, t) \sin(\theta)\, \mathrm{d}\theta\, \mathrm{d}\varphi$ of finding a particle with orientation $\hat{\mathbf{D}}$ within $\mathrm{d}\theta$ about θ and within $\mathrm{d}\varphi$ about φ at time t obeys the Debye equation [21]

$$\frac{\partial}{\partial t} P(\hat{\mathbf{D}}, t) = D_0^{\mathrm{r}} \nabla_\omega^2 P(\hat{\mathbf{D}}, t) \tag{3}$$

where ∇_ω^2 is the angular part of the Laplace operator ∇^2 and D_0^{r} is the Stokes–Einstein–Debye rotational diffusion coefficient. In rotational-FRAP, linearly polarized light is used for the bleach and probe beams. The absorption (bleaching and excitation) as well as emission has a transition dipole moment, which implies that the dye molecules have a preferred orientation for absorption and emission. They are characterized by unit vectors $\hat{\mu}_{\mathrm{B}}$, $\hat{\mu}_{\mathrm{A}}$ and $\hat{\mu}_{\mathrm{E}}$ in the frame of reference of the dye molecule. The corresponding absorption dipole moments $\hat{\mu}_{\mathrm{B}}$ and $\hat{\mu}_{\mathrm{A}}$ are virtually identical since the bleach and probe beam have the same wavelength (532 nm) here.

The polarization state of an electromagnetic (em) wave is represented by the direction of the electric field component. In a polarized FRAP experiment three polarization directions are important. The polarization direction of the bleach and

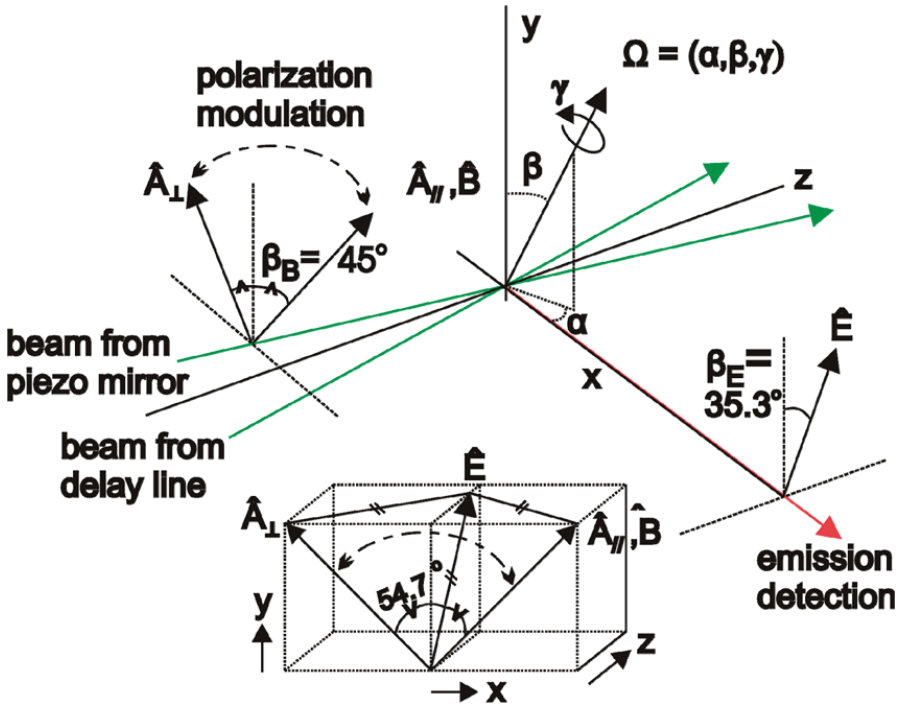

Figure 2. Sketch of the experimental polarization geometry. The sample is located at the origin. The orientations Ω of the dye molecules are described by the three Euler angles, $\Omega \equiv (\alpha, \beta, \gamma)$. The polarization of the probe beam $\hat{\mathbf{A}}$ is modulated between the two extreme orthogonal linear polarization states, $\beta_{\hat{\mathbf{A}}_\parallel} = +45°$ and $\beta_{\hat{\mathbf{A}}_\perp} = -45°$ with respect to the vertical direction. The inset at the bottom of the drawing shows that the angle between B, $\hat{\mathbf{A}}_\parallel$ or $\hat{\mathbf{A}}_\perp$ on one hand and $\hat{\mathbf{E}}$ on the other equals 54.7°.

probe beams will be denoted by the unit vectors $\hat{\mathbf{B}}$ and $\hat{\mathbf{A}}$, respectively (see figure 2). The fluorescence emission is measured through a polarization filter with an orientation $\hat{\mathbf{E}}$. The fluorescence intensity $I_f(t, t', t'')$ measured in a rotational-FRAP experiment can be described by integration over space $\mathbf{r}$ extended for the integration over the orientations Ω at time t and Ω_0 at time t_0 of the dye molecules

$$\begin{aligned} I_f(t, t', t'') = A(t)\, Q N_p \int \mathrm{d}\Omega_0 \int \mathrm{d}\Omega \int_V \mathrm{d}\mathbf{r}_0 \\ \times \int_V \mathrm{d}\mathbf{r}\, n(\mathbf{r}_0, \hat{\mathbf{B}}, \Omega_0, t_0) \\ \times I_p(\mathbf{r}, t') P(\mathbf{r}_0, \Omega_0, t_0) P(\mathbf{r}, \Omega, t | \mathbf{r}_0, \Omega_0, t_0) \\ \times P_A(\Omega, t'') P_E(\Omega) \end{aligned} \quad (4)$$

where time t'' (much shorter than t' and t) is added for later use to describe the modulation of the polarization direction. $P_A(\Omega, t'')$ and $P_E(\Omega)$ are the probabilities for a dye molecule to absorb or respectively to emit a photon, as we will see later. $P(\mathbf{r}, \Omega, t|\mathbf{r}_0, \Omega_0, t_0)$ is the conditional probability density function for particles that, given a certain particle was at position $\mathbf{r}_0$ and with orientation Ω_0 at t_0, will be found at position $\mathbf{r}$ and with orientations Ω at time t. Furthermore, $P(\mathbf{r}_0, \Omega_0, t_0)$ is the equilibrium probability density function (pdf) for a particle at time t_0 to have position $\mathbf{r}_0$ and orientation Ω_0. In an isotropic system a molecule can be found with equal probability at any given orientation, leading to $P(\mathbf{r}_0, \Omega_0, t_0) = 1/(4\pi V)$. The orientation Ω is expressed in terms of three Euler angles α, β and γ, as defined in figure 2 (see vector labeled Ω at the position of the origin).

The bleach pulse at time t_0 changes the distribution of the unbleached dye from an isotropic orientation distribution to an anisotropic distribution $n(\mathbf{r}_0, \hat{\mathbf{B}}, \Omega_0, t_0)$ that depends on $\hat{\mathbf{B}}$. It is assumed that during the short bleach pulse (5 ns) the particles with dye do not reorientate. The probability $P_B(\Omega_0)$ that a dye molecule with an absorption dipole moment in direction $\hat{\mu}_B$ absorbs a photon with polarization $\hat{\mathbf{B}}$ produced by the bleach beam is proportional to

$$P_B(\Omega_0) \propto |\hat{\mu}_B(\Omega_0) \cdot \hat{\mathbf{B}}|^2. \quad (5)$$

The distribution of unbleached dye molecules assuming a first-order bleaching reaction is given by [18]

$$n(\mathbf{r}_0, \hat{\mathbf{B}}, \Omega_0, t_0) = n_0 \exp[-\alpha I_b(\mathbf{r}_0) |\hat{\mu}_B(\Omega_0) \cdot \hat{\mathbf{B}}|^2 \Delta t_b]. \quad (6)$$

Assuming that the initial system in equilibrium is statistically invariant under translation, the initial orientation Ω_0 distribution is independent of the initial position $\mathbf{r}_0$. Since for shallow bleaches the exponent between braces in equation (6) is much smaller than 1, the exponent can be replaced by a first-order Taylor expansion

$$n(\mathbf{r}_0, \hat{\mathbf{B}}, \Omega_0, t_0) = n_0[1 - K P_B(\Omega_0, t_0) R(\mathbf{r}_0, t_0)] \quad (7)$$

where the exponent has been factorized in a term proportional to the orientation-dependent bleach probability $P_B(\Omega_0, t_0)$ (cosine squared distribution, conform equation (5)), and a position-dependent factor $R(\mathbf{r}_0, t_0)$. This cosine squared distribution implies a cylindrically symmetric

pdf $P(\mathbf{r}_0, \hat{\mathbf{B}}, \Omega_0, t_0)$ about $\hat{\mathbf{B}}$ at each position in the illuminated area if the initial orientation Ω_0 distribution is isotropic. In the case of deep bleaches, the orientational distribution of bleached dye widens but retains its cylindrical symmetry.

The probability $P_A(\Omega, t'')$ that a dye molecule absorbs a photon with polarization $\hat{\mathbf{A}}(t'')$ produced by the polarization modulated probe beam is equivalent to the expression in equation (5):

$$P_A(\Omega, t'') \propto |\hat{\mu}_A(\Omega) \cdot \hat{\mathbf{A}}(t'')|^2. \tag{8}$$

Since the polarization direction of the probe beam is modulated, this probability does not only depend on the dynamics of the particle orientation on time t, but also on the time dependence of the modulation t'' (see later). The probability of emission of a photon with polarization $\hat{\mathbf{E}}$ is denoted as $P_E(\Omega)$ and is given by

$$P_E(\Omega) \propto |\hat{\mu}_E(\Omega) \cdot \hat{\mathbf{E}}|^2. \tag{9}$$

We define the bleach contrast as

$$\Delta I_f(t) \equiv I_f(t) - I_f(t < 0) \tag{10}$$

i.e. the difference between fluorescence intensity at time t after the pulse and the pre-bleach intensity $I_f(t < 0)$. Inserting equations (4) and (7) into equation (10) gives

$$\begin{aligned}\Delta I_f(t, t', t'') = -A(t) QKN_p n_0 \int d\Omega_0 \int d\Omega \int_V d\mathbf{r}_0 \\ \times \int_V d\mathbf{r}\, P_B(\Omega_0, t_0)\, R(\mathbf{r}_0, t_0) \\ \times I_p(\mathbf{r}, t') P(\mathbf{r}_0, \Omega_0, t_0) P(\mathbf{r}, \Omega, t|\mathbf{r}_0, \Omega_0, t_0) \\ \times P_A(\Omega, t'') P_E(\Omega).\end{aligned} \tag{11}$$

Inserting equations (5), (8) and (9) into equation (11) leads to the following expression for the bleach contrast

$$\begin{aligned}\Delta I_f(t, t', t'') = -A(t) QKN_p n_0 \int d\Omega_0 \int d\Omega \int_V d\mathbf{r}_0 \int_V d\mathbf{r} \\ \times R(\mathbf{r}_0, t_0)\, I_p(\mathbf{r}, t') P(\mathbf{r}_0, \Omega_0, t_0) \\ \times P(\mathbf{r}, \Omega, t|\mathbf{r}_0, \Omega_0, t_0) |\hat{\mu}_B(\Omega_0) \cdot \hat{\mathbf{B}}|^2 \\ \times |\hat{\mu}_A(\Omega) \cdot \hat{\mathbf{A}}(t'')|^2 |\hat{\mu}_E(\Omega) \cdot \hat{\mathbf{E}}|^2.\end{aligned} \tag{12}$$

The experimental geometry (see figure 2) is chosen such that the polarization dependence of the fluorescence emission is eliminated. This condition is fulfilled if the angle between the polarization of the bleach beam $\hat{\mathbf{B}}$ and the orientation $\hat{\mathbf{E}}$ of the polarizer in front of the detector is $\beta_{EB} = 54.7°$. In this case the second-order Legendre polynomial term $P_2(\beta_{EB}) = (3\cos^2\beta_{EB} - 1)/2$ which is part of the final expression [8, 18] for the bleach contrast is reduced to zero. This is achieved by keeping the polarization of the bleach beam $\hat{\mathbf{B}}$ constant at an angle $\beta_B = 45°$ from the vertical, and by observing the emission through a polarizer with the polarization direction $\hat{\mathbf{E}}$ oriented at a so-called magic angle $\beta_E = 35.3°$ from the vertical (see figure 2).

The polarization of the probe beam is modulated by a photoelastic modulator (PEM), between two extreme orthogonal linear polarization states, parallel ($\hat{\mathbf{A}} \parallel \hat{\mathbf{B}}$) and perpendicular ($\hat{\mathbf{A}} \perp \hat{\mathbf{B}}$) to the polarization of the bleach beam, with corresponding bleach contrast $\Delta I_{f_\parallel}$ and $\Delta I_{f_\perp}$, respectively.

A PEM, orientated at an angle $\beta_{PEM} = 45°$, gives a sinusoidal retardation between two orthogonal components with a phase amplitude ψ_{ret} of π radians ($\lambda/2$) of:

$$\delta_{PEM} = \psi_{ret} \sin(2\pi f_{PEM} t''). \tag{13}$$

The incident light beam has a polarization direction of $\beta_{inc.} = 0°$. The effect is a rotation of the polarization direction of the light beam over an angle of $2(\beta_{PEM} - \beta_{inc.}) = 90°$ at times t'' of the maximum positive ('fast') induced retardation $\lambda/2$, and analogously a rotation of $-90°$ at times t'' of minimum negative ('slow') induced retardation $-\lambda/2$. Note that the polarization states of these two extremes are in fact the same. At times t'' of zero crossing (unstrained element, see section 4) the light has an unaltered polarization ($\beta = 0°$). In between, the light is elliptically polarized. The polarization direction is in this way modulated twice per modulation period ($2f_{PEM}$, typically 100 kHz) between two extreme orthogonal linear polarization directions, vertical ($\beta = 0°$) and horizontal ($\beta = 90°$).

The polarization state of the beam can be described by Jones vectors $\hat{\mathbf{E}}$, which are normalized to unit length if the base $[|E_x|\, e^{i\varphi_x}, |E_y|\, e^{i\varphi_y}]$ is used [22]. This vector is then $\tilde{\mathbf{E}}_0 = (0, 1)$ for the incidence laser beam. The effect of an optical element can be described by a 2×2 Jones matrix with complex elements, which is for the PEM using equation (13) for the retardation δ_{PEM},

$$\mathbf{M}_{PEM} = \begin{pmatrix} e^{[i\delta_{PEM}]} & 0 \\ 0 & 1 \end{pmatrix} = \begin{pmatrix} e^{[i\psi_{ret}\ \sin(2\pi f_{PEM} t'')]} & 0 \\ 0 & 1 \end{pmatrix}. \tag{14}$$

Since the fast and slow axes of the PEM have an orientation of $\beta_{PEM} = 45°$, rotation matrices $\mathbf{R}$ are used to transform the polarization state from the laboratory frame of reference to the PEM reference system (and backwards)

$$\begin{aligned}\tilde{\mathbf{E}}_\psi &= \mathbf{R}(-\beta_{PEM}) \cdot \mathbf{M}_{PEM} \cdot \mathbf{R}(\beta_{PEM}) \cdot \tilde{\mathbf{E}}_0 \\ &= \begin{pmatrix} \cos(-\beta_{PEM}) & \sin(-\beta_{PEM}) \\ -\sin(-\beta_{PEM}) & \cos(-\beta_{PEM}) \end{pmatrix} \\ &\quad \times \begin{pmatrix} e^{[i\psi_{ret}\ \sin(2\pi f_{PEM} t'')]} & 0 \\ 0 & 1 \end{pmatrix} \\ &\quad \times \begin{pmatrix} \cos(\beta_{PEM}) & \sin(\beta_{PEM}) \\ -\sin(\beta_{PEM}) & \cos(\beta_{PEM}) \end{pmatrix} \begin{bmatrix} 0 \\ 1 \end{bmatrix}.\end{aligned} \tag{15}$$

For the Jones vector $\tilde{\mathbf{E}}_\psi$ of the beam emerging from the PEM this gives:

$$\begin{aligned}\tilde{\mathbf{E}}_\psi = \tfrac{1}{2} \begin{pmatrix} e^{[i\psi_{ret}\ \sin(2\pi f_{PEM} t'')]} - 1 \\ e^{[i\psi_{ret}\ \sin(2\pi f_{PEM} t'')]} + 1 \end{pmatrix} = e^{[i(\psi_{ret}/2)\ \sin(2\pi f_{PEM} t'')]} \\ \times \begin{pmatrix} i\sin[(\psi_{ret}/2)\ \sin(2\pi f_{PEM} t'')] \\ \cos[(\psi_{ret}/2)\ \sin(2\pi f_{PEM} t'')] \end{pmatrix}.\end{aligned} \tag{16}$$

The overall phase factor in front of the vector on the right-hand side can be ignored, since this factor does

not change the state of polarization, or the normalized intensity $I \propto \left|\tilde{\mathbf{E}}^*_\psi \cdot \tilde{\mathbf{E}}_\psi\right|$. At times t'', where the argument $[(\psi_{\rm ret}/2)\ \sin(2\pi f_{\rm PEM}t'')]$ equals $\pm\pi/2$, the light is polarized in the horizontal direction. The phase factor i in front of the x-component is only related to the phase of the em wave, which cycles many times during one modulation period. If the argument is zero, the polarization stays vertical. The intensity I is proportional to the sum of intensities of the horizontal (x) component and the vertical (y) component [23]

$$\begin{aligned} I \propto \left|\tilde{\mathbf{E}}^*_\psi \cdot \tilde{\mathbf{E}}_\psi\right| &= I_x + I_y \\ &= T_x\{1 - \cos[\psi_{\rm ret}\ \sin(2\pi f_{\rm PEM}t'')]\} \\ &\quad + T_y\{1 + \cos[\psi_{\rm ret}\ \sin(2\pi f_{\rm PEM}t'')]\} \end{aligned} \tag{17}$$

with T_x and T_y the total transmission factors of the optical train (including the fluorescence process) for the x- and vertical y-component.

The Fourier transform of $\cos[\psi_{\rm ret}\sin(2\pi f_{\rm PEM}t'')]$ in equation (17) can be expanded in a series Bessel functions of the first kind J_n with $\phi_0 = 0$

$$\begin{aligned} \cos[\phi_0 + \psi_{\rm ret}\sin(2\pi f_{\rm PEM}t'')] &= \cos(\phi_0)J_0(\psi_{\rm ret}) \\ &\quad + 2\sum_{n=1}^{\infty}\{\cos(\phi_0)\cos[(2n)2\pi f_{\rm PEM}t''] \\ &\quad \times J_{2n}(\psi_{\rm ret}) - \sin(\phi_0)\sin[(2n-1)2\pi f_{\rm PEM}t''] \\ &\quad \times J_{2n-1}(\psi_{\rm ret})\}. \end{aligned} \tag{18}$$

Both intensities I_x and I_y can be described by the even order Bessel function with frequency $2nf_{\rm PEM}$. $J_0(\psi_{\rm ret})$ is a constant ('dc') background term. In the case of linear dichroism (T_x not equal to T_y), a $2f_{\rm PEM}$ component appears in the signal since the cosine terms in equation (17) do not cancel. This can be measured with a lock-in amplifier. Note that if one inserted a linear polarizer along the horizontal (x) direction, I_x is measured. The retardation amplitude $\psi_{\rm ret}$ is set to a value slightly beyond π radians to optimize the anisotropy signal.

Although the used multi-layer dielectric mirrors and beam splitter are (almost) nonpolarizing in the sense of intensity, they intrinsically exhibit a distinguished phase lag $\Delta\varphi_{\rm m}$ for mirror m between the s- (perpendicular, also called *senkrecht*) and p- (parallel) polarization direction with respect to the plane of incidence. The total phase lag is $\sum_{\rm m}\Delta\varphi_{\rm m}$. To keep the polarization state well defined in polarized FRAP, care is taken that the two extreme orthogonal linear polarization states are kept parallel to the s- and, respectively, p- directions of the mirrors $(E_x, E_y) = (E_{\rm s}, E_{\rm p})$ by modulating the polarization direction between the vertical ($\beta = 0°$) and horizontal ($\beta = 90°$) direction. After the reflections by the mirrors, using equation (16), the Jones vector is:

$$\begin{aligned} \tilde{\mathbf{E}}_{\rm after\ mirrors} &= \begin{pmatrix} |r_s|\ \mathrm{e}^{\left[\mathrm{i}\sum_{\rm m}\Delta\varphi_{\rm m}\right]} & 0 \\ 0 & |r_{\rm p}| \end{pmatrix}\begin{pmatrix} E_s \\ E_{\rm p} \end{pmatrix} \\ &= \begin{pmatrix} \mathrm{i}\,|r_s|\,\mathrm{e}^{\left[\mathrm{i}\sum_{\rm m}\Delta\varphi_{\rm m}\right]}\sin\left[\dfrac{\psi_{\rm ret}}{2}\ \sin(2\pi f_{\rm PEM}t'')\right] \\ |r_{\rm p}|\ \cos\left[\dfrac{\psi_{\rm ret}}{2}\ \sin(2\pi f_{\rm PEM}t'')\right] \end{pmatrix}. \end{aligned} \tag{19}$$

The reflection coefficients $|r_s|$ and $|r_{\rm p}|$ are added to take into account the equivalent of linear dichroism caused by the difference in the reflection by the mirrors of the s- and p-polarization states, which induces an offset in the polarization anisotropy measurement. The phase factor caused by the mirrors expressed by the exponent in front of the x-component in equation (19) is only related to the phase of the em wave and is unimportant when the argument of the subsequent sine term is $\pm\pi/2$, since then the y component is zero.

Lastly, the polarization state is rotated over an angle of 45° by a fixed $\lambda/2$ retardation plate oriented at an angle $\beta_{\lambda/2} = 22.5°$ in front of the sample, to arrive at the desired extreme polarization directions of 45° and −45°, respectively (and a polarization direction of $\beta_B = 45°$ for the unmodulated bleach beam). For the Jones vector for the beam at the position of the sample this gives:

$$\begin{aligned} \tilde{\mathbf{E}}_{\rm sample\ in} &= \begin{pmatrix} \cos(-\beta_{\lambda/2}) & \sin(-\beta_{\lambda/2}) \\ -\sin(-\beta_{\lambda/2}) & \cos(-\beta_{\lambda/2}) \end{pmatrix}\begin{pmatrix} -1 & 0 \\ 0 & 1 \end{pmatrix}_{\lambda/2} \\ &\quad \times \begin{pmatrix} \cos(\beta_{\lambda/2}) & \sin(\beta_{\lambda/2}) \\ -\sin(\beta_{\lambda/2}) & \cos(\beta_{\lambda/2}) \end{pmatrix} \\ &\quad \times \begin{pmatrix} \mathrm{i}\,|r_s|\,\mathrm{e}^{\left[\mathrm{i}\sum_{\rm m}\Delta\varphi_{\rm m}\right]}\sin\left[\dfrac{\psi_{\rm ret}}{2}\ \sin(2\pi f_{\rm PEM}t'')\right] \\ |r_{\rm p}|\ \cos\left[\dfrac{\psi_{\rm ret}}{2}\ \sin(2\pi f_{\rm PEM}t'')\right] \end{pmatrix}. \end{aligned} \tag{20}$$

With the substitution $\beta_{\lambda/2} = 22.5°$ we obtain for $\tilde{\mathbf{E}}_{\rm sample\ in}$:

$$\frac{1}{2}\sqrt{2}\begin{pmatrix} \mathrm{i}\,|r_s|\,\mathrm{e}^{\left[\mathrm{i}\sum_{\rm m}\Delta\varphi_{\rm m}\right]}\sin\left[\dfrac{\psi_{\rm ret}}{2}\ \sin(2\pi f_{\rm PEM}t'')\right] \\ \quad + |r_{\rm p}|\ \cos\left[\dfrac{\psi_{\rm ret}}{2}\ \sin(2\pi f_{\rm PEM}t'')\right] \\ \mathrm{i}\,|r_s|\,\mathrm{e}^{\left[\mathrm{i}\sum_{\rm m}\Delta\varphi_{\rm m}\right]}\sin\left[\dfrac{\psi_{\rm ret}}{2}\ \sin(2\pi f_{\rm PEM}t'')\right] \\ \quad - |r_{\rm p}|\ \cos\left[\dfrac{\psi_{\rm ret}}{2}\ \sin(2\pi f_{\rm PEM}t'')\right] \end{pmatrix}. \tag{21}$$

The polarization state sweeps between +45° (in which case the extra phase factor does not change the intensity) and −45° with respect to the vertical direction as can be seen from equation (21) with $|r_s| \approx |r_{\rm p}|$.

The bleach contrast of the dc component in the fluorescence intensity $\Delta I_{\rm dc}(t)$ can be defined similar to equation (10) as

$$\Delta I_{\rm dc}(t) \equiv I_{\rm dc}(t) - I_{\rm dc}(t < 0) \tag{22}$$

where $I_{\rm dc}(t)$ is the recovered fluorescence intensity after the bleach pulse and $I_{\rm dc}(t < 0)$ is the pre-bleach intensity. The bleach contrast is time dependent mainly due to a combination of reversible bleaching, contained in a factor $A(t)$ in equations (2) and (12), and translational exchange diffusion to and from the exterior of the fringe area. The bleach contrast can be normalized by the pre-bleach intensity corrected for

the dark current of the detector

$$\Delta I'_{\rm dc}(t) = \frac{I_{\rm dc}(t) - I_{\rm dc}(t<0)}{I_{\rm dc}(t<0) - I_{\rm dc,dark}}. \quad (23)$$

The polarization anisotropy in the fluorescence intensity due to the linear dichroism (*in casu* of the absorption dipole moment caused by the polarized bleach beam) is proportional to the envelope of the periodic component expressed by the (signed) scalar $I_{{\rm LIA},\upsilon}(t)$ in the signal measured with a lock-in amplifier at reference frequency ν (=$2f_{\rm PEM}$)

$$\Delta I_\upsilon(t) \equiv I_{\upsilon,\parallel}(t'') - I_{\upsilon,\perp}(t'') = -I_{{\rm LIA},\upsilon}(t) \quad (24)$$

where $I_{\upsilon,\parallel}(t'')$ and $I_{\upsilon,\perp}(t'')$ are the intensities with the polarization direction of the probe beam parallel and perpendicular to the polarization direction of the bleach beam. This expression can be normalized by the pre-bleach intensity corrected for the dark current (since for our case $I_{{\rm dc},\parallel}(t<0) = I_{{\rm dc},\perp}(t<0)$ in the expression in [8]) to find the normalized polarization anisotropy

$$\Delta I'_\upsilon(t) = \frac{-I_{{\rm LIA},\upsilon}(t)}{I_{\rm dc}(t<0) - I_{\rm dc,dark}}. \quad (25)$$

Care must be taken that both the numerator and denominator are on the same absolute scale by taking into account the gain of the lock-in amplifier and conversion from rms to peak-to-peak value. The above-mentioned factor $A(t)$ is also contained in $\Delta I_\upsilon(t)$.

The polarization anisotropy is defined as

$$r(t) \equiv \frac{\Delta I'_\parallel(t) - \Delta I'_\perp(t)}{\Delta I'_{\rm tot}(t)} = \frac{\Delta I'_\upsilon(t)}{\Delta I'_{\rm tot}(t)} \quad (26)$$

where $\Delta I'_{\rm tot}(t)$ is introduced to make $r(t)$ independent of the contribution of the above-mentioned time-dependent factor $A(t)$, as well as an experimental time-independent factor Q in equation (12):

$$\Delta I'_{\rm tot}(t) = \Delta I'_\parallel(t) + 2\Delta I'_\perp(t). \quad (27)$$

With $\Delta I'_{\rm dc}(t) = [\Delta I'_\parallel(t) + \Delta I'_\perp(t)]/2$ and from equation (24) normalized: $\Delta I'_\upsilon(t) = \Delta I'_\parallel(t) - \Delta I'_\perp(t)$, we arrive at

$$\Delta I'_{\rm tot}(t) = 3\Delta I'_{\rm dc}(t) - \tfrac{1}{2}\Delta I'_\upsilon(t). \quad (28)$$

From the normalized data we find from equations (26) and (28):

$$r(t) = \frac{\Delta I'_\upsilon(t)}{3\Delta I'_{\rm dc}(t) - \frac{1}{2}\Delta I'_\upsilon(t)}. \quad (29)$$

In section 3.2 a comparison is made between the polarization anisotropy calculated in equation (29) from the experimental data and the rotational diffusion coefficients.

3. Dynamics of ellipsoids

3.1. Rotational diffusion

A rotation of an ellipsoid (see figure 3) can be decomposed into rotations around its three principal axes. The rotational relaxation time τ characterizes the Brownian angular movement of particles. In principle, the orientation of the ellipsoids can be aligned, for example by an external field (not used here), with their axis $\boldsymbol{i}$ parallel to the vertical z-axis that is fixed in the laboratory frame of reference. Brownian motion will disorient the particles when the external field is switched off at time $t = 0$. The orientation of any ellipsoid at time t can be described by the cosine of the angle θ between the axis $\boldsymbol{i}$ and the z-axis. When the ensemble-averaged value of $\cos(\theta)$ has fallen to e^{-1}, the time that has elapsed is defined as the rotational relaxation time τ_i. Since the ellipsoid can move in any direction, the rotational relaxation time τ_a of the long principal axis $\boldsymbol{a}$ around the remaining two axes $\boldsymbol{b}$ and $\boldsymbol{c}$ depends on the rotational diffusion coefficient of the latter two principal axes (see figure 3), which are equal for an ellipsoid of revolution ($a \neq b = c$).

Thus τ_a is given by:

$$\tau_a = \frac{1}{D^{\rm r}_b + D^{\rm r}_c} = \frac{1}{2\,D^{\rm r}_\perp}. \quad (30)$$

The rotation relaxation times of the two short (equatorial) axes are equal for an ellipsoid of revolution

$$\tau_b = \frac{1}{D^{\rm r}_a + D^{\rm r}_c} = \frac{1}{D^{\rm r}_\parallel + D^{\rm r}_\perp} (=\tau_c). \quad (31)$$

The rotational friction coefficients of ellipsoids are described in the seminal articles of Perrin [24, 25] with a correction given by Koenig [26] (see appendix C in the supplementary material online available at stacks.iop.org/JPhysCM/24/245101/mmedia). The hydrodynamic volume $V_{\rm hydro}$ is often larger than the geometrical volume of an ellipsoid of revolution, which equals $V_{\rm geometric} = (4/3)\pi ab^2$. For a rigid ellipsoid of revolution with a hydrodynamic volume $V_{\rm hydro}$ in a solvent with viscosity η, there are two Stokes–Einstein–Debye rotational diffusion coefficients, which for stick boundary conditions are given by the relations [27, 28]

$$D^{\rm r}_\parallel = \frac{k_{\rm B}T}{6\eta V_{\rm hydro} g_\parallel} \quad (32)$$

for rotation around the long symmetry axis (see figure 3(a)), and

$$D^{\rm r}_\perp = \frac{k_{\rm B}T}{6\eta V_{\rm hydro} g_\perp} \quad (33)$$

for rotation around the short (equatorial) axes of the long axis itself, where $k_{\rm B}$ is Boltzmann's constant and T the absolute temperature.

In equations (32) and (33) the Perrin factors $g_\parallel$ and $g_\perp$ quantify the deviation from the rotational diffusion coefficient $D^{\rm r}_{\rm sphere} = k_{\rm B}T/6\eta V_{\rm hydro}$ of a sphere with the same volume as the ellipsoid in question. The Perrin factors g_i depend solely on the aspect ratio, $p = a/b$, and are given by [27]

$$g_\parallel = \frac{2(p^2-1)}{3p(p-S)}; \qquad g_\perp = \frac{2(p^4-1)}{3p\,[(2p^2-1)\,S - p]}. \quad (34)$$

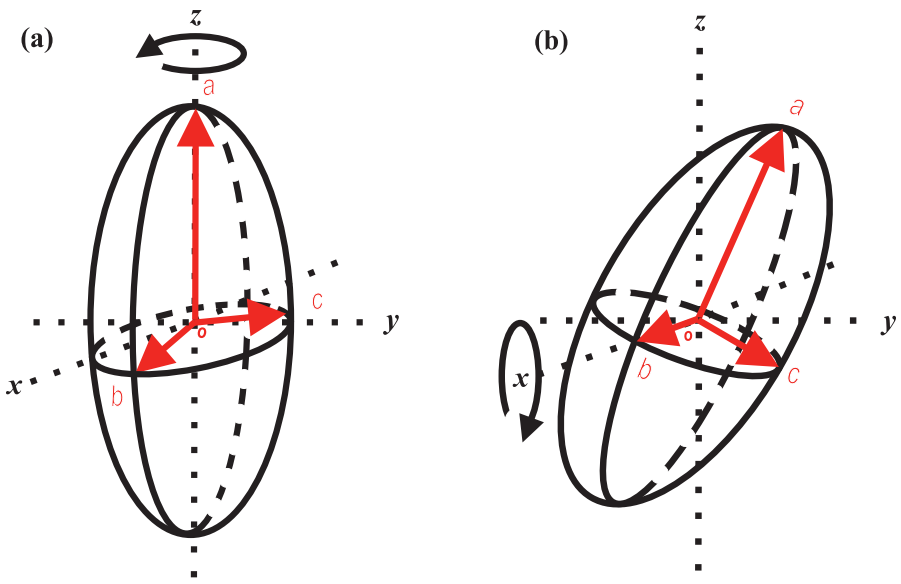

Figure 3. Rotation of short axes ***b*** and ***c*** around the long (symmetry) axis ***a*** (in figure (a)) and of short axis ***c*** and long axis ***a*** around axis ***b*** (in figure (b)).

For a prolate ellipsoid of revolution ($a > b$) the term S is given by the analytic expression [27]

$$S_{\text{prolate}} = \frac{1}{\sqrt{p^2-1}} \ln\left[p + \sqrt{p^2-1}\right] \tag{35}$$

whereas for an oblate ellipsoid of revolution ($a < b$) [27]

$$S_{\text{oblate}} = \frac{1}{\sqrt{1-p^2}} \arctan\left[p^{-1}(1-p^2)^{1/2}\right]. \tag{36}$$

The rotational diffusion coefficient $D^{\text{r}}_{\parallel}$ is weakly dependent on the aspect ratio p, as is expected for the rotation around the long symmetry axis. On the other hand, $D^{\text{r}}_{\perp}$ is strongly dependent on the aspect ratio p for prolate ellipsoids. Note that the Perrin factors in equation (34) equal $g_i = 1$ in the limit of an aspect ratio of $p = 1$ (spherical particles); the proof is given in appendix B (in the supplementary material online available at stacks.iop.org/JPhysCM/24/245101/mmedia) for $g_{\parallel}$.

3.2. Rotational correlation functions

In the case of isotropic colloidal particles, the polarization anisotropy $r(t)$ can be expressed as [8]

$$r(t) = 5r_0\langle P_2[\hat{D}(t)\cdot\hat{D}(0)]\rangle \tag{37}$$

where r_0 is the initial anisotropy, which depends on the orientation of the absorption dipole moment of the dye molecules with respect to the colloids, the residual mobility (on time scales much smaller than used here) of the dye molecules inside the colloidal particles, and a number of experimental factors. P_2 is the second-order Legendre polynomial and its argument $\hat{D}(t)\cdot\hat{D}(0)$ is the cosine of the angle through which the particle rotates during a time t. The ensemble-averaged term in equation (37) is the rotational (or orientational) correlation function. With the solution of the Debye equation (see equation (3)), the ensemble-average in equation (37) for a sphere is [8]

$$r(t) = 5r_0\langle P_2[\hat{D}(t)\cdot\hat{D}(0)]\rangle = r_0 \mathrm{e}^{-6D^{\text{r}}_0 t} \tag{38}$$

which is a single-exponential decay as opposed to the case of an anisotropic particle, which is discussed below.

Theoretically [29], the decay of the polarization anisotropy $r(t)$ as defined in equation (26) for an ellipsoid of revolution is given by a sum of three exponentials [14, 30]

$$\frac{r(t)}{r_0} = 0.4\,\mathrm{e}^{-\frac{t}{\phi_1}} + 0.4\,\mathrm{e}^{-\frac{t}{\phi_2}} + 0.2\,\mathrm{e}^{-\frac{t}{\phi_3}}. \tag{39}$$

The rotational correlation times ϕ_i in equation (39) are the eigenvalues of the rotational diffusion equation [31] and are related to the rotational diffusion coefficients $D^{\text{r}}_{\parallel}$ and $D^{\text{r}}_{\perp}$ given by equations (32) and (33)

$$\phi_1 = \frac{1}{4D^{\text{r}}_{\parallel} + 2D^{\text{r}}_{\perp}} \tag{40}$$

$$\phi_2 = \frac{1}{D^{\text{r}}_{\parallel} + 5D^{\text{r}}_{\perp}} \tag{41}$$

$$\phi_3 = \frac{1}{6D^{\text{r}}_{\perp}}. \tag{42}$$

Evidently, the rotational correlation times ϕ_i are not the same as the rotational relaxation times τ_i belonging to the rotation of the principal axes of the ellipsoid. The apparent rotational diffusion coefficient is not the algebraic average of D^{r}_i belonging to the principal axes, as opposed to the case of the translational diffusion in the long time limit.

In the case of an asymmetric (or general) ellipsoid ($a \neq b \neq c$), the polarization anisotropy $r(t)$ is the sum of five exponentials and there is no analytic expression for the rotational friction factors, but they can be determined by calculating elliptical integrals numerically. The polarization

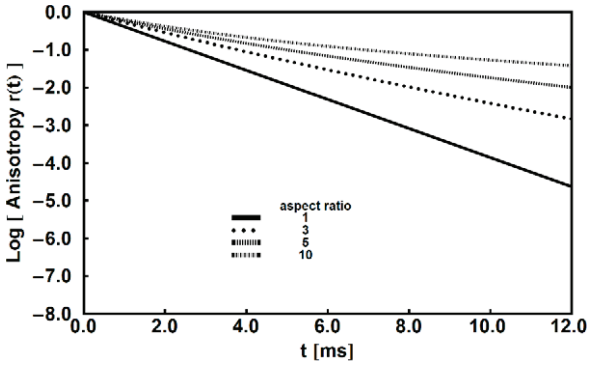

Figure 4. Rotational correlation functions from equation (39) for different aspect ratios p and a constant volume V_{hydro} of the ellipsoid of revolution.

anisotropy in equation (39) is normalized by the initial anisotropy r_0 at $t = 0$. The exponential amplitudes in equation (39) have the given numerical value [16] because it is assumed that the ellipsoids are labeled with the dye transition dipole moments orientated randomly. In general, the amplitudes depend on the orientation of the absorption and emission dipole moment inside the ellipsoid when the dye molecules have a preferred orientation with respect to the frame of reference of the ellipsoid, and also on the rotational diffusion coefficients for asymmetric ellipsoids.

The theoretical rotational correlation function is plotted in figure 4 for different values of the aspect ratio p. For a rigid spherical particle (aspect ratio $p = 1$), the rotational correlation function is a single-exponential decay. Since the Perrin factors (equation (34)) in the expression for the rotational diffusion coefficients depend on the aspect ratio p in a different way, the rotational correlation times ϕ_i are different from each other for non-spherical ellipsoids of revolution. In that case, the shape of the rotational correlation function in a logarithmic plot deviates quite a lot from a straight line. At a large aspect ratio ($p \gg 5$) the parallel and perpendicular rotational diffusion coefficients are substantially different. In the limit of larger time t the decay is then dominated by the rotational correlation time ϕ_3 and only the perpendicular rotational diffusion coefficient has to be taken into account as has been done by Bereolos [32]. Note that the decay time depends strongly on the volume V_{hydro} of the ellipsoid.

3.3. Translational diffusion

The translational diffusion coefficient for a prolate ellipsoid of revolution which obeys the stick boundary condition has been given by Happel and Brenner [33] with S_{prolate} from equation (35)

$$D^{\text{t}} = \frac{k_{\text{B}} T S_{\text{prolate}}}{6\pi\eta b}. \tag{43}$$

This translational diffusion coefficient D^{t} of a Brownian ellipsoid of revolution in an isotropic phase is the orientational average [34] of the translational diffusion coefficients $D^{\text{t}}_{\parallel}$ and $D^{\text{t}}_{\perp}$. Note that S_{prolate} in equation (43) equals 1 in the limit of an aspect ratio of $p = 1$ (spherical particles), in which case we obtain the Stokes–Einstein relation for a sphere.

This expression (43) can be coupled in the fit procedure with equations (32) and (33).

4. Experiments

4.1. Instrumental setup

4.1.1. Excitation. The bleach pulses are generated by a frequency-doubled neodymium:yttrium aluminum garnet laser (Nd:YAG, Continuum Minilite II, see figure 5) at a wavelength $\lambda_B = 532$ nm with a pulse duration of 5 ns. The maximum bleach energy used in our setup is 15 mJ/pulse. The spatial coherence length of this laser is 10 mm [35].

The probe beam is produced by a continuous wave diode pumped solid state neodymium:yttrium vanadate laser (Nd:YVO_4, Cobolt Samba) at a wavelength $\lambda_A = 532$ nm. This laser is operated in single longitudinal mode at a power of 15 mW maximum. The coherence length is typically more than 10 m. The beam pointing stability is better than 10 μrad $^{\circ}\text{C}^{-1}$. By a neutral density filter (labeled nd in figure 5), the probe beam intensity can be controlled. For both λ_B and λ_A the absorption cross section of the dye rhodamine isothiocyanate (RITC) is 44% in comparison with the maximum of RITC at a wavelength of 564 nm in a silica matrix [36].

The bleach and probe laser initially have a vertical polarization ($\beta = 0^{\circ}$). This is more accurately optimized by a Glan–Taylor polarizer (labeled pol1 in figure 5) for the bleach beam and a Glan–Thompson polarizer (labeled pol2 in figure 5) for the probe beam. Both the bleach and probe laser beam are split in two by the same nonpolarizing, all-dielectric, single laser line, high energy plate beamsplitter (CVI BSNP532-50-2025) with a diameter of 50.8 mm, at an incidence angle of 45°. The transmitted and reflected beams are equal as far as the intensities are concerned in order to obtain interference fringes with a high visibility. The piezo-electric modulator (Burleigh PZ-91) is a mirror mounted on a piezo-electric element with a working range of 0–2 μm and a low hysteresis. After the bleach pulse, the dc offset is adjusted to obtain a spatial phase of the probe fringe with respect to the bleach fringe of $\varphi_0 = \pi/2$, which is optimal when modulation is used. The split beam is recombined in the center of the sample by this piezomirror at a distance in the order of 1 m under a semiangle θ of 2.7° typically (see figure 1). Thus, a fringe pattern with a spacing L of 5.7 μm was obtained, which can be altered between 2 and 15 μm by changing θ by realignment. The modulation frequency ξ_{piezo} is adjusted to 675 Hz.

4.1.2. Beam optics. The ray matrix theory for Gaussian beam optics with ABCD matrices including complex beam parameters [37] has been used for the design. Both the bleach and probe laser beams are focused in the center of the sample to the same fringe area size with a beam waist radius w_0 of 160 μm to avoid fluorescence from unbleached areas. The number of fringes in this area is typically 43,

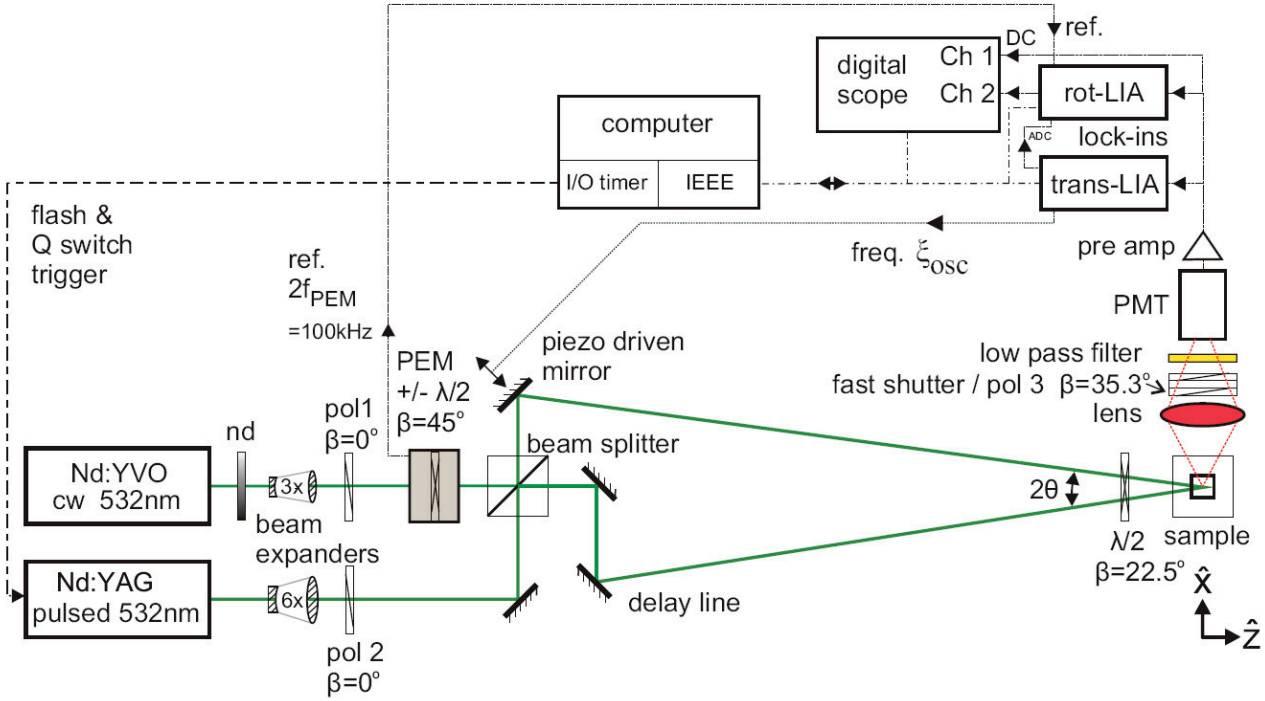

Figure 5. Schematic diagram of the combined rotational and translational-FRAP setup. The abbreviation $\lambda/2$ denotes half-lambda platelets; pol are polarizers; nd is a neutral density filter, and β the orientation angle with respect to the vertical direction. The various components of the setup are further discussed in 4.1.1–4.1.5.

which ensures that the approximation in equation (2) for the fluorescence intensity can be used for the analysis of the translational-FRAP part.

Beam expanders have to be applied as otherwise the diffraction of light obstructs the creation of such a small spot on a large distance. Galilean type beam expanders are used [22], giving an expansion of the diameter of the laser beam of 6× for the bleach and 3× for the probe beam. The distance between the two lenses of the beam expanders is adjusted such that the exit beam is not collimated (infinite conjugate), but focused in the center of the sample. The depth of focus, i.e. the distance at which the beam radius $w = 1.05w_0$, is 7.5 mm for the bleach beam and 48 mm for the probe beam. The distance at which the intersecting beams start to overlap is 4 mm in front of the position of maximum overlap cross section, which is larger than the optical path length (maximum 3 mm) inside the sample cell. Since the coherence length of the pulsed bleach laser is only 10 mm, an optical delay line (see figures 1 and 5) is inserted in the fixed optical path ($\boldsymbol{k_1}$ in figure 1). In this way the optical path length Λ between the beam splitter and sample is the same for both beams within 10 mm. An additional advantage is that the focal points of both beams coincide, since the image distances after the beamsplitter become equal. For the coarse alignment, a pinhole was used with a diameter of 200 μm on the position of the sample. The near optical field at the sample position was investigated by a magnified projection of the intensity distribution over the area of the pinhole on a screen at a large distance. As the overlap of the beams at the sample position is very critical, the mirror in the delay line beam is equipped with actuators (Picomotors, New Focus Inc.) to fine-tune the tilts by remote control. The mirrors used in the piezomirror and delay line are all mirrors with a diameter of 50.4 mm (large, in order to transmit the expanded beams) optimized for an incidence angle of 45°.

A prerequisite for FRAP measurements is the stability of the whole setup since movements on the micrometer scale are measured. Therefore, the optical part of the setup as schematically depicted in figure 5 is contained in a polystyrene shielding box, built on an air-pressured optical table which damps mechanical vibrations.

4.1.3. Modulation of polarization. Modulation of the probe polarization direction $\hat{\mathbf{A}}(t'')$ is obtained by a Photo Elastic Modulator (PEM, Hinds International Inc., model 80, see figure 5) giving a sinusoidal phase lag, at a frequency $f_{\mathrm{PEM}} =$ 50 kHz and with a phase retardation amplitude of slightly more than a half-wave ($\lambda/2$). In the PEM, a sound wave in a rectangular bar of fused silica is used to provide a sinusoidal retardation modulation of the polarization of the probe beam. The fast and slow axis of this induced retardation are oriented at an angle of $\beta_{\mathrm{PEM}} = 45°$ with respect to the vertical direction (see discussion in equation (21)). In front of the sample, a quartz half-wave retardation plate (labeled $\lambda/2$ in figure 5; Melles Griot 02WRQ027 for 532 nm) with an orientation of the fast axis at $\beta_{\lambda/2} = 22.5°$ turns the orthogonal linear polarization directions over a polar angle of 45° to the desired +45° for the bleach beam and ±45° for the probe beam with respect to the vertical direction.

4.1.4. Detection. Colloidal fluids to be measured are contained in square borosilicate glass cells (Vitrocom CS103)

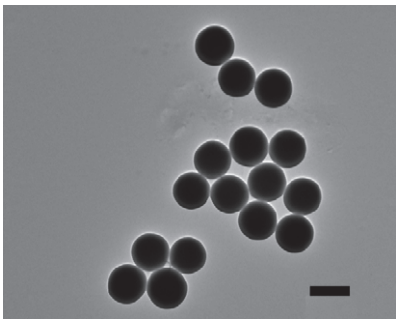

Figure 6. TEM image of isotropic silica particles [36] (code Sisol). Scale bar = 400 nm.

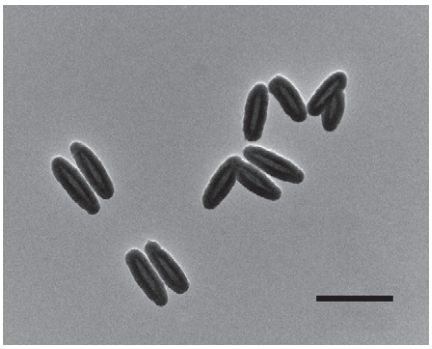

Figure 7. Representative TEM image of hollow silica colloidal ellipsoids of revolution (code A5H) used for a typical integrated FRAP measurement on anisotropic particles. Scale bar = 400 nm. For more information on the preparation and properties of these colloids see [39, 40].

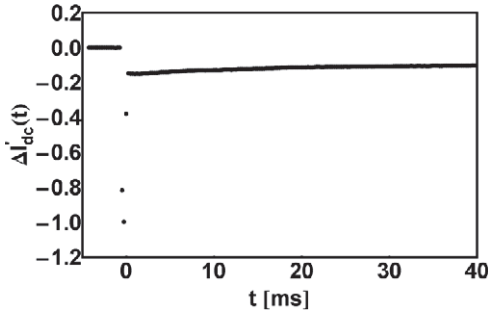

Figure 8. Normalized bleach contrast $\Delta I'_{dc}(t)$ according to equation (23) of photobleaching measurement on colloidal spheres. On time zero the shutter is closed shortly to protect the detector. Initially, 15% of the dye molecules are bleached.

with an optical path length of 3 mm and a height of 48 mm. The fluorescent light is detected at right angles to the bisector of the intersecting beams by a photo multiplier tube (PMT; Products For Research, cooled with a Peltier element to reduce the dark current) as shown in figure 5. In front of the detector a polarizer is set to the so-called magic angle of $\beta_E = 35.3°$ (see figure 2). This polarizer is actually a component of the fast ferroelectric liquid crystal (FLC) shutter (Displaytech LV2500AC with driver DR95FLC), which is used to protect the sensitive detector from scattered light and the luminescence burst during the intense bleach pulse. For this purpose, the PMT also has an internal gating circuit, which disables the PMT's internal electron multiplier during the bleach pulse. The shutter has a total switching open time of 70 μs [8], which limits the shortest time scale accessible in the rotational-FRAP experiments. The fluorescent light is collected by a lens in front of the detector. An optical filter (Andover, 600FS40-50) used as a low pass filter is inserted to separate the fluorescent light from the scattered light.

4.1.5. Signal processing. The output signal current from the PMT is amplified with a large dynamic range current to voltage amplifier (Melles Griot, 13 AMP003). The frequency component at the polarization modulation frequency $2f_{\mathrm{PEM}}$ is measured by a lock-in amplifier (labeled rot-LIA in figure 5; Signal Recovery, model 7265) for the rotational part of the FRAP setup. The reference signal is obtained from the $2f_{\mathrm{PEM}}$ reference output of the PEM driver.

By the oscillator of the translational lock-in amplifier (labeled trans-LIA in figure 5), the piezomirror is modulated with a frequency ξ_{piezo}. The output of the rot-LIA is fed to channel 2 of a fast digital oscilloscope (LeCroy LT322). Via two A/D converters, the x and y output of the (analog) trans-LIA is stored in a buffer of the (full digital) rot-LIA. The dc signal in the detector output is measured with channel 1 of the fast digital oscilloscope. To avoid mutual influence, the frequency of the polarization modulation ($2f_{\mathrm{PEM}} =$ 100 kHz) is chosen much higher than the frequency of the fringe modulation ($\xi_{\mathrm{piezo}} = 675$ Hz). The (integration) time constant of both the rot-LIA and trans-LIA are adjusted to 1/30 of the expected decay time of the relating correlation function. During the integration time of the trans-LIA, many modulation periods of the polarization modulations have been passed (and averaged). The amplitude of the small ac 'ripple' (<0.25%) due to the fringe or polarization modulation is small as compared to the total intensity. As the frequencies of the modulation of the rotational and translational part of the setup are not correlated, the effect of the fringe modulation is also suppressed by averaging many runs.

In the past, continuous wave lasers were used in translational-FRAP for the bleaching with bleaching times of at least 0.5 s [20]. In our setup with bleaching by a pulsed laser with a short pulse duration (5 ns), the noise is the limit for the shortest accessible measuring time in translational-FRAP. To obtain sufficient statistical accuracy for both the rotational- and translational-FRAP, each measurement consists of several runs. To achieve this, the sample is moved down to fresh, unbleached areas before each bleach pulse. To accomplish this, a sample translation stage (Newport M-UTM100CC1DD) is used, which has a range of 100 mm, a resolution of 1 μm, and is controlled with a universal motion controller (Newport, model ESP300).

4.2. Sample preparation

For the proof of principle measurement with isotropic particles, spherical silica particles (code Sisol) with a fluorescent core and a shell of bare silica were used (see figure 6) synthesized by Verhaegh [36]. The dye rhodamine

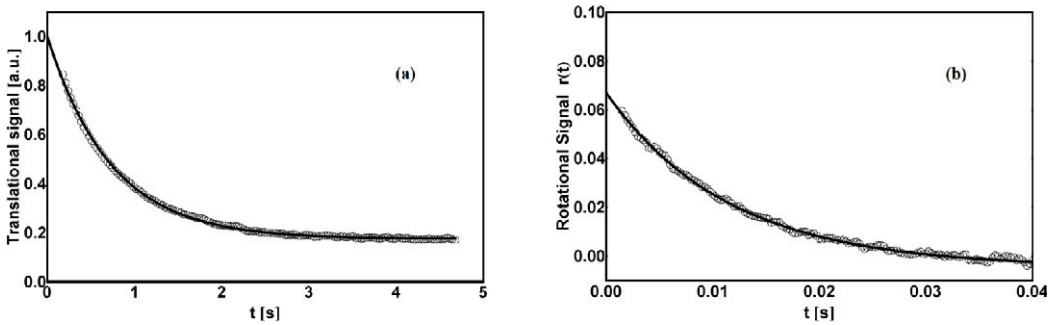

Figure 9. Simultaneous measurement (circles) of translational (a) and rotational (b) diffusion of silica spheres ($R_{\text{hydro}} = 229$ nm), with concentration of 0.7% dispersed in DMF, in an integrated FRAP setup. The solid lines denote a least squares exponential fit. The translational part of the FRAP measurement has been done at a reciprocal length of $k_0 = 1.1 \times 10^6$ m^{-1}.

B 5-isothiocyanate (RITC) is covalently bonded to the silica in the core. Typical dye contents are 6.6×10^4 dye molecules per particle core, which means an average dye–dye distance in the order of 4 nm. The TEM outer radius of the Sisol particles is 189 nm, which is twice the core size, and the polydispersity is 14%. The shell is added to screen interactions between dye molecules on the surface of the colloid core and its environment. RITC has its excitation maximum at a wavelength of 564 nm in a silica matrix and its emission maximum around 580 nm. The Sisol particles were dispersed in dimethylformamide (DMF) in which they have a hydrodynamic radius R_{hydro} of 229 nm measured with rotational- (only) FRAP by Koenderink *et al* [38].

For the integrated FRAP measurement of anisotropic particles, hollow silica colloidal ellipsoids of revolution labeled with RITC have been used (code A5H, see figure 7), synthesized by Sacanna *et al* [39, 40]. The TEM size is 345 nm ($2a$) for the long axis and 118 nm ($2b$) for the short axis with a relative statistical standard deviation of 12% and 4%, respectively. The ellipsoids were freshly redispersed in an (almost) refractive-index matching mixture (2:3 v/v) of DMF and dimethyl sulfoxide (DMSO) from a stable stock dispersion of those particles in ethanol.

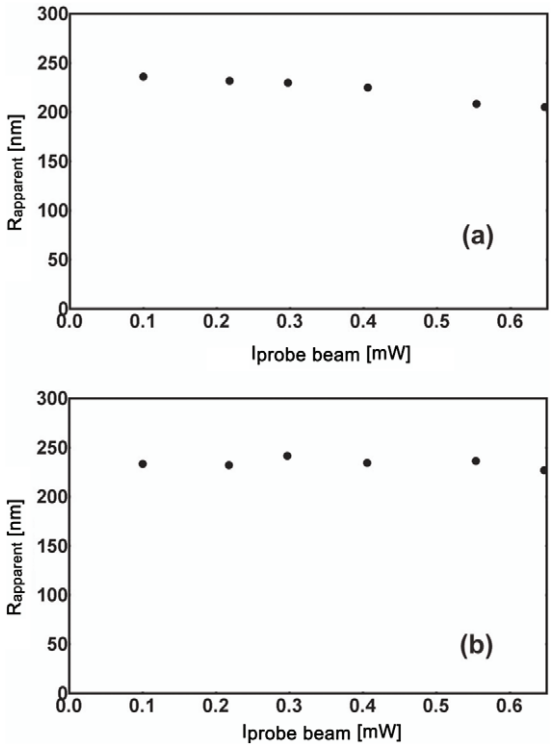

Figure 10. Effect of probe beam intensity $I_{\text{probe beam}}$ on the apparent radius R_{apparent} of RITC-labeled silica spheres ($R_{\text{hydro}} = 229$ nm) in DMF measured with the integrated translational- (a) rotational- (b) FRAP setup.

5. Application and discussion

5.1. Simultaneous measurement of rotational and translational diffusion of spherical colloids

As a proof of principle, simultaneous measurements of rotational and translational Brownian diffusion of isotropic colloids with the integrated FRAP have been performed on colloidal spherical particles (code Sisol, see figure 6). Figure 8 shows the time-dependent contrast, normalized by the pre-bleach fluorescence intensity, $\Delta I'_{\text{dc}}(t)$ defined in equation (23) of the recovery of the fluorescence after bleaching on time $t = 0$ s. Initially 15% of the dye molecules had been bleached.

The translational-FRAP decay (self-intermediate scattering function) in figure 9(a) and polarization anisotropy $r(t)$ in figure 9(b) were measured simultaneously. As can be seen two correlation functions are obtained in contrast to depolarized DLS. The semiangle between the intersecting beams was adjusted to $\theta = 2.7°$, which gives a fringe spacing of 5.7 μm, corresponding to a reciprocal length of $k_0 = 1.1 \times 10^6$ m^{-1}. Both curves show a single-exponential decay and are fitted by standard fitting procedures (Mathematica program, Wolfram). The characteristic decay time of the translational part is 0.73 ± 0.05 s, giving a translational diffusion coefficient of $D^{\text{t}}_{\text{apparent}} = 1.17 \times 10^{-12}$ m^2 s^{-1}, which is corrected for the polydispersity and the viscosity is corrected for the temperature. Via the Stokes–Einstein relation an apparent hydrodynamic radius of $R_{\text{hydro}} = 239$ nm is obtained. As observed also in the past [20], the translational-FRAP curve in figure 9(a) has a non-zero baseline which must be an artifact for which we have no explanation yet.

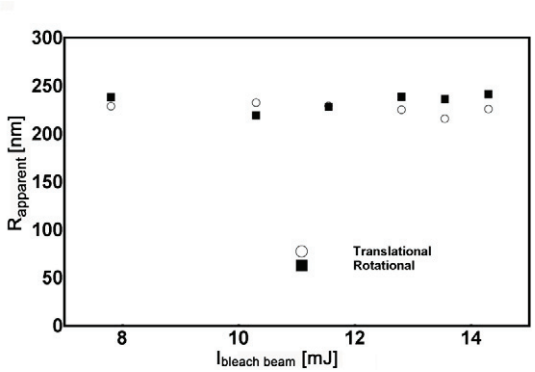

Figure 11. Effect of bleach beam intensity $I_{\text{bleach beam}}$ in terms of pulse energy on the apparent radius R_{apparent} of RITC-labeled silica spheres ($R_{\text{hydro}} = 229$ nm) in DMF measured with the integrated translational–rotational-FRAP setup.

The anisotropy of the rotational part of the FRAP measurement $r(t)$ has a characteristic decay time of 11.5 ± 0.4 ms. From this a rotational diffusion coefficient $D^{\text{r}}_{0,\text{apparent}} = 15.3\ \text{s}^{-1}$ corrected for the polydispersity [38] is obtained. Using the Stokes–Einstein–Debye relation, an apparent hydrodynamic radius of $R_{\text{hydro}} = 236$ nm can be calculated.

The apparent radii found in the translational part and, respectively, rotational part of the FRAP setup agree well between themselves. Although the apparent radii are on average 26% larger than the TEM radius, they are similar to the values reported by Koenderink [38]: $R_{\text{hydro}} = 215$ nm in ethanol with DLS and $R_{\text{hydro}} = 229$ nm in DMF in another rotational (only) FRAP setup.

The initial polarization anisotropy r_0 in equation (38) was around 0.07 (see intercept in figure 9(b)), which is on the same level as values in the literature for colloids with dye molecules [19]. The small negative value of the baseline of the polarization anisotropy in figure 9(b) most likely is an artifact for which we have no explanation at the moment.

The influence of the probe beam intensity $I_{\text{probe beam}}$ on the apparent radius of the RITC-labeled silica spheres (code Sisol) has been investigated in the range of 0.1–0.65 mW (figure 10). For the translational part of the integrated FRAP setup in figure 10(a) a smaller apparent size tendency can be seen when the probe beam intensity increases. This effect might be attributed to convection due to local heating. In a trial experiment, where a probe laser beam with a considerable intensity was shone on the surface of a sedimentation layer of the spherical particles with dye, it was demonstrated that an upward convective transport of particles started. The effect of this vertical velocity due to convection is a more rapid decay of translational-FRAP curves [20].

The coefficient of determination R^2 as a measure for the goodness of fit of the translational decay curve decreases at probe beam intensities smaller than 0.04 mW (data not shown) due to a low signal to noise ratio at low intensities. In the probe intensity range under consideration in figure 10(b) for the rotational part of the simultaneous measurement, no trend in the apparent radius can be distinguished.

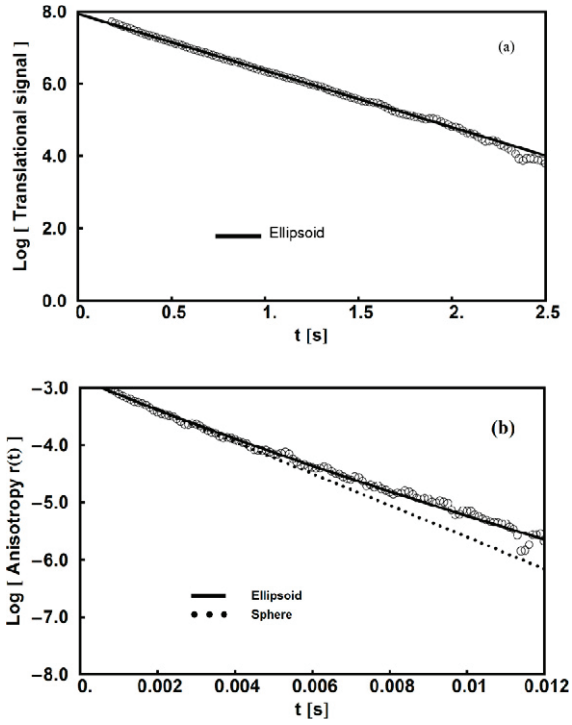

Figure 12. Simultaneous FRAP measurement of ellipsoids of revolution. The translational-FRAP curve (circles in figure (a)) should display a single-exponential decay, in accordance with the theory (solid line in figure (a)), see equations (2) and (43). The measured rotational-FRAP curve of the polarization anisotropy (circles in figure (b)) should yield a three-exponential decay (figure (b) solid line for an aspect ratio of 3.1). For comparison, the polarization anisotropy of a sphere with an equivalent volume is added in figure (b) (dotted line). The translational part of the FRAP measurement has been done at a reciprocal length of $k_0 = 1.1 \times 10^6\ \text{m}^{-1}$.

This observation supports the above-mentioned assumption regarding the convection effect in translational-FRAP. A probe beam intensity higher than 0.3 mW should be avoided to prevent convection. From the analysis of the rotational-FRAP curves in the probe intensity range of figure 10, the initial polarization anisotropy r_0 in equation (39) appears to be constant (data not shown).

The effect of the bleach beam pulse energy in units of mJ on the integrated FRAP measurements is shown in figure 11 for the translational and rotational part. The lower limit of the pulse energy is limited by the trigger threshold of the data acquisition whereas the maximum pulse energy is limited by the damage threshold of the optical parts. In the range of figure 11 the apparent radii are almost constant, i.e. independent of the bleach intensity. From the analysis of the rotational-FRAP curves in the bleach intensity range of figure 11, the polarization anisotropy r_0 (see equation (39)) shows no significant variation (data not shown).

Although the measured translational and rotational diffusion coefficients do not vary much in these series of probe and bleach intensities, these intensities need to be optimized for each combination of particles, incorporated dye concentration, and solvent.

5.2. Simultaneous measurement of translational and rotational diffusion of anisotropic colloids

A typical example of a simultaneous FRAP measurement on rhodamine-labeled colloidal ellipsoids of revolution is shown in figure 12. The hollow rigid particles (code A5H) [39, 40] were dispersed with a volume concentration of 2.8% v/v in a mixture of DMSO and DMF (3:2 v/v). The TEM size (see also figure 7) is 345 nm for the long axis dimension ($2a$, which is twice the length of the semi-axis of symmetry $|\boldsymbol{a}|$) and 118 nm for the short axis dimension ($2b$) and relative standard deviations of 12% and 4%, respectively.

Although these particles are anisotropic, a single-exponential decay is expected for the long time translational diffusion limit according to equations (2) and (43). The translational diffusion coefficient D^{t} is only weakly dependent on the aspect ratio p (see equation (43)). Therefore the translational-FRAP curve is initially fitted with an aspect ratio p from the TEM measurement ($p_{\mathrm{TEM}} = \langle 2a\rangle/\langle 2b\rangle = 2.9$). The hydrodynamic volume is calculated from this fit, giving the length of the long and short axis. This is used in the analysis of the rotational-FRAP curve (polarization anisotropy), from which the apparent aspect ratio p is derived. Use is made of the fact that the deviation of this curve (see figure 12(b) circles) from a single-exponential curve (see figure 12(b) dotted line) belonging to the rotational-FRAP curve of an equivalent (in the sense of initial slope) sphere is strongly dependent on the aspect ratio p. The measured rotational-FRAP curve of the polarization anisotropy of an ellipsoid of revolution (circles in figure 12(b)) has to give a three-exponential decay (solid line in figure 12(b) for an aspect ratio p of 3.1) in the case of the experimental polarization geometry used here. The best matching aspect ratio p is iteratively used in the fit of the translational-FRAP curve. According to this procedure the hydrodynamic volume is derived from the translational diffusion coefficient measured in the translational part of the integrated FRAP setup. This gives an apparent ensemble-averaged size of 467 nm for the long axis dimension ($2a$) and 151 nm for the short axis dimension ($2b$). From the simultaneous measured rotational-FRAP curve an apparent aspect ratio p of 3.1 has been obtained. Although the size of the symmetry axis is, respectively, 35% and 28% larger than the TEM sizes for the long and short axis of the ellipsoids of revolution under consideration, the same order of magnitude of deviation (26%) was found in section 5.1 for the integrated FRAP measurement on isotropic particles. Part of the high size values might be ascribed to the polydispersity, for which no correction is taken into account yet for this analysis of integrated FRAP measurement on ellipsoids. The apparent aspect ratio p from the analysis of the rotational part of the simultaneous measurement ($p = 3.1$) deviates 5% from the aspect ratio from the TEM measurement. The iteratively fitted method mentioned above has to be regarded as a first approximation. In a more advanced method the translational and rotational analysis could be mathematically coupled and a correction for the polydispersity, with the appropriate weighting factors [38, 41] which are different for rotational and translational-FRAP respectively, has to be incorporated. Clearly the length of the long and short principle axis of the ellipsoids of revolution with a low aspect ratio p ($p = 3.1$) as used here, can be measured in one combined measurement which is hard to do with a rotational only FRAP setup.

6. Conclusions

We have demonstrated in a proof of principle experiment that we succeeded in developing a method for simultaneous measurement of rotational and translational diffusion of anisotropic colloids with this integrated fluorescence recovery after photobleaching (FRAP) setup. These two dynamic processes are measured under exactly the same conditions and at the same time in dynamic experiments, which can later be used in e.g. measurements on sedimentation–diffusion profiles. Two correlation functions are obtained in one single measurement in contrast to depolarized dynamic light scattering. The diffusion processes can be measured on a time scale of sub-milliseconds for the rotational part to minutes or more for both the rotational and translational part. In our FRAP setup a modulated fringe pattern is used for the translational part, and a photoelastic modulator for the polarization modulation.

We measured combined FRAP on silica ellipsoids of revolution as an example of anisotropic particles. We found the expected single-exponential decay of the translational-FRAP curve for long time translational Brownian diffusion. The rotational-FRAP curve of ellipsoids of revolution matches the three-exponential decay in the case of the experimental polarization geometry used here, where only the absorption dipole moment orientation is measured, making the analysis simpler. From the simultaneously measured translational diffusion coefficient, the hydrodynamic volume V_{hydro} can be calculated, which establishes together with the aspect ratio p from the rotational part of the FRAP measurement both the length of the long and short axes.

The measured ensemble-averaged size of the long and short principle axes of the ellipsoids of revolution is obtained with a hydrodynamic-to-TEM-size ratio of the same order of magnitude as measured in dynamic light scattering and rotational only FRAP equipment. For the aspect ratio of the ellipsoids used here (around 3) we took advantage of measuring translational and rotational dynamics at one time, as the long and short axis length are very difficult to derive from a translational- or rotational-FRAP only experiment.

Acknowledgments

We thank M P Lettinga, G Koenderink, and A Imhof for the helpful discussions at the early stages of this project. Also, thanks to N A M Verhaegh for synthesizing the silica spheres, and S Sacanna and L Rossi for providing the colloidal ellipsoids of revolution. J C Heesen and P M van den Beld from the instrumental department are acknowledged for adaptation of the optical components.

References

[1] Imhof A, van Blaaderen A, Maret G and Dhont J G K 1994 A comparison between the long-time self-diffusion and low shear viscosity of concentrated dispersions of charged colloidal silica spheres *J. Chem. Phys.* **100** 2170–81

[2] Peters R, Peters J, Tews K H and Bahr W 1974 Microfluorimetric study of translational diffusion in erythrocyte-membranes *Biochim. Biophys. Acta* **367** 282–94

[3] Lanni F, Taylor D L and Ware B R 1981 Fluorescence photobleaching recovery in solutions of labeled actin *Biophys. J.* **35** 351–64

[4] Chatenay D, Urbach W, Messager R and Langevin D 1987 Self-diffusion of interacting micelles: FRAP study of micelles self-diffusion *J. Chem. Phys.* **86** 2343–51

[5] Bu Z and Russo P S 1994 Diffusion of dextran in aqueous (hydroxypropyl) cellulose *Macromolecules* **27** 1187–94

[6] Gorti S, Plank L and Ware B R 1984 Determination of electrolyte friction from measurements of tracer diffusion coefficients, mutual diffusion coefficients, and electrophoretic mobilities of charged spheres *J. Chem. Phys.* **81** 909–14

[7] Davoust J, Devaux P F and Leger L 1982 Fringe pattern photobleaching, a new method for the measurement of transport-coefficients of biological macromolecules *EMBO J.* **1** 1233–8

[8] Lettinga M P, Koenderink G H, Kuipers B W M, Bessels E and Philipse A P 2004 Rotational dynamics of colloidal spheres probed with fluorescence recovery after photobleaching *J. Chem. Phys.* **120** 4517–29

[9] Lettinga M P, van Kats C M and Philipse A P 2000 Rotational diffusion of tracer spheres in packings and dispersions of colloidal spheres studied with time-resolved phosphorescence anisotropy *Langmuir* **16** 6166–72

[10] Lettinga M P, van Zandvoort M A M J, van Kats C M and Philipse A P 2000 Phosphorescent colloidal silica spheres as tracers for rotational diffusion studies *Langmuir* **16** 6156–65

[11] Koenderink G H, Lettinga M P and Philipse A P 2002 Rotational dynamics of charged colloidal spheres: role of particle interactions *J. Chem. Phys.* **117** 7751–64

[12] Dhont J K G 1996 *An Introduction to Dynamics of Colloids* (Amsterdam: Elsevier)

[13] Pfleiderer P, Milinkovic K and Schilling T 2008 Glassy dynamics in monodisperse hard ellipsoids RID A-4950-2009 *Europhys. Lett.* **84** 16003

[14] Small E W and Isenberg I 1977 Hydrodynamic properties of a rigid molecule: rotational and linear diffusion and fluorescence anisotropy *Biopolymers* **16** 1907–28

[15] Kang K, Gapinski J, Lettinga M P, Buitenhuis J, Meier G, Ratajczyk M, Dhont J K G and Patkowski A 2005 Diffusion of spheres in crowded suspensions of rods *J. Chem. Phys.* **122** 044905

[16] Lakowicz J R 2006 *Principles of Fluorescence Spectroscopy* (New York: Springer)

[17] Tinland B, Meistermann L and Weill G 2000 Simultaneous measurements of mobility, dispersion, and orientation of DNA during steady-field gel electrophoresis coupling a fluorescence recovery after photobleaching apparatus with a fluorescence detected linear dichroism setup *Phys. Rev.* E **61** 6993–8

[18] Wegener W A and Rigler R 1984 Separation of translational and rotational contributions in solution studies using fluorescence photobleaching recovery *Biophys. J.* **46** 787–93

[19] Velez M and Axelrod D 1988 Polarized fluorescence photobleaching recovery for measuring rotational diffusion in solutions and membranes *Biophys. J.* **53** 575–91

[20] Imhof A 1996 Dynamics of concentrated colloidal dispersion *PhD Thesis* Utrecht University

[21] Debye P 1929 *Polar Molecules* (New York: Dover)

[22] Hecht E 1998 *Optics* (Reading, MA: Addison-Wesley)

[23] Born M and Wolf E 2001 *Principles of Optics* (Cambridge: Cambridge University press)

[24] Perrin F 1934 Mouvement Brownian d'un ellipsoide (I) dispersion dielectrique pour des molecules ellipsoidales *J. Physique* VII **5** 497–510

[25] Perrin F 1936 Mouvement Brownian d'un ellipsoide (II): rotation libre et depolarisation des fluorescences; translation et diffusion de molecules ellipsoidales *J. Physique* VII **7** 1–11

[26] Koenig S H 1975 Brownian motion of an ellipsoid. A correction to Perrin's results *Biopolymers* **14** 2421–3

[27] Ferrer M L, Duchowicz R, Carrasco B, de la Torre J G and Acuna A U 2001 The conformation of serum albumin in solution: a combined phosphorescence depolarization-hydrodynamic modeling study *Biophys. J.* **80** 2422–30

[28] Mateo C R, Lillo M P, Brochon J C, Martínez-Ripoll M, Sanz-Aparicio J and Acuña A U 1993 Rotational dynamics of 1,6-diphenyl–1,3,5-hexatriene and derivatives from fluorescence depolarization *J. Phys. Chem.* **97** 3486–91

[29] Ehrenberg M and Rigler R 1972 Polarized fluorescence and rotational Brownian motion *Chem. Phys. Lett.* **14** 539–44

[30] Menning R 1961 Theorie der fluoreszenzpolarisation fur nicht kugelsymmetrische molekule *Z. Phys. Chem. Neue Folge* **28** 168–89

[31] Wahl P 1983 Fluorescence anisotropy decay and Brownian rotational motion: theory and application in biological systems *Time-Resolved Fluorescence Spectroscopy in Biochemistry and Biology (NATO ASI Series A69)* ed R B Cundall and R E Dale (New York: Plenum) pp 497–521

[32] Bereolos P, Talbot J, Allen M P and Evans G T 1993 Transport properties of the hard ellipsoid fluid *J. Chem. Phys.* **99** 6087–97

[33] Happel J and Brenner H 1973 *Low Reynolds Number Hydrodynamics: With Special Applications to Particulate Media* (Leiden: Nordhoff)

[34] Han Y, Alsayed A M, Nobili M, Zhang J, Lubensky T C and Yodh A G 2006 Brownian motion of an ellipsoid *Science* **314** 626–30

[35] Lauterborn W, Kurz T and Wiesenfeldt M 1999 *Coherent Optics* (Berlin: Springer)

[36] Verhaegh N A M and Van Blaaderen A 1994 Dispersions of rhodamine-labeled silica spheres-synthesis, characterization, and fluorescence confocal scanning laser microscopy *Langmuir* **10** 1427–38

[37] Silvast W T 2004 *Laser Fundamentals* (Cambridge: Cambridge University Press)

[38] Koenderink G H 2003 *Rotational and Translational Diffusion in Colloidal Mixtures* (Utrecht: Utrecht University)

[39] Sacanna S, Rossi L, Kuipers B W M and Philipse A P 2006 Fluorescent monodisperse silica ellipsoids for optical rotational diffusion studies *Langmuir* **22** 1822–7

[40] Sacanna S, Rossi L, Wouterse A and Philipse A P 2007 Observation of a shape-dependent density maximum in random packings and glasses of colloidal silica ellipsoids *J. Phys.: Condens. Matter* **19** 376108

[41] Martchenko I, Dietsch H, Moitzi C and Schurtenberger P 2011 Hydrodynamic properties of magnetic nanoparticles with tunable shape anisotropy: prediction and experimental verification *J. Phys. Chem.* B **115** 14838–45

Appendix (supplementary material online)

A. Derivation of intensity of fringe pattern in translational-FRAP

The intensity of the fringe pattern is proportional to the square of the superposition of the real parts of the electric field strengths of the two split beams of which the time average is give by [35]

$$I(\mathbf{r},t') = \frac{1}{2}\varepsilon_0 c\,\mathbf{E}(\mathbf{r})\cdot\mathbf{E}(\mathbf{r})^* = \frac{1}{2}\varepsilon_0 c\,(\mathbf{E}_1(\mathbf{r})+\mathbf{E}_2(\mathbf{r},t'))\cdot(\mathbf{E}_1(\mathbf{r})+\mathbf{E}_2(\mathbf{r},t'))^*. \quad \text{(A1)}$$

Using equation 2.1 in ref Imhof [20] for $\mathbf{E}_1$ and $\mathbf{E}_2$, we find

$$\begin{aligned} I(\mathbf{r},t') = \frac{1}{2}\varepsilon_0 c\,(&\frac{1}{\sqrt{2}}\mathbf{E}_0\, e^{\left[-\frac{\mathbf{r}\cdot(\mathbf{I}-\hat{\mathbf{k}}_1\hat{\mathbf{k}}_1)\cdot\mathbf{r}}{w^2}\right]} e^{[i(\mathbf{k}_1\cdot\mathbf{r})]} + \frac{1}{\sqrt{2}}\mathbf{E}_0\, e^{\left[-\frac{\mathbf{r}\cdot(\mathbf{I}-\hat{\mathbf{k}}_2\hat{\mathbf{k}}_2)\cdot\mathbf{r}}{w^2}\right]} e^{[i(\mathbf{k}_2\cdot\mathbf{r}+\varphi(t'))]}) \\ \times(&\frac{1}{\sqrt{2}}\mathbf{E}_0\, e^{\left[-\frac{\mathbf{r}\cdot(\mathbf{I}-\hat{\mathbf{k}}_1\hat{\mathbf{k}}_1)\cdot\mathbf{r}}{w^2}\right]} e^{[i(\mathbf{k}_1\cdot\mathbf{r})]} + \frac{1}{\sqrt{2}}\mathbf{E}_0\, e^{\left[-\frac{\mathbf{r}\cdot(\mathbf{I}-\hat{\mathbf{k}}_2\hat{\mathbf{k}}_2)\cdot\mathbf{r}}{w^2}\right]} e^{[i(\mathbf{k}_2\cdot\mathbf{r}+\varphi(t'))]})^*. \end{aligned} \quad \text{(A2)}$$

This gives

$$\begin{aligned} I(\mathbf{r},t') = \frac{1}{2}\varepsilon_0 c(&\frac{1}{2}\mathbf{E}_0\mathbf{E}_0{}^*\, e^{\left[-\frac{2\mathbf{r}\cdot(\mathbf{I}-\hat{\mathbf{k}}_1\hat{\mathbf{k}}_1)\cdot\mathbf{r}}{w^2}\right]} + \frac{1}{2}\mathbf{E}_0\mathbf{E}_0{}^*\, e^{\left[-\frac{2\mathbf{r}\cdot(\mathbf{I}-\hat{\mathbf{k}}_2\hat{\mathbf{k}}_2)\cdot\mathbf{r}}{w^2}\right]} \\ &+\frac{1}{2}\mathbf{E}_0\mathbf{E}_0{}^*\, e^{\left[-\frac{\mathbf{r}\cdot(\mathbf{I}-\hat{\mathbf{k}}_1\hat{\mathbf{k}}_1)\cdot\mathbf{r}}{w^2}\right]} e^{\left[-\frac{\mathbf{r}\cdot(\mathbf{I}-\hat{\mathbf{k}}_2\hat{\mathbf{k}}_2)\cdot\mathbf{r}}{w^2}\right]} e^{[i((\mathbf{k}_1-\mathbf{k}_2)\cdot\mathbf{r}-\varphi(t'))]} \\ &+\frac{1}{2}\mathbf{E}_0{}^*\mathbf{E}_0\, e^{\left[-\frac{\mathbf{r}\cdot(\mathbf{I}-\hat{\mathbf{k}}_1\hat{\mathbf{k}}_1)\cdot\mathbf{r}}{w^2}\right]} e^{\left[-\frac{\mathbf{r}\cdot(\mathbf{I}-\hat{\mathbf{k}}_2\hat{\mathbf{k}}_2)\cdot\mathbf{r}}{w^2}\right]} e^{[-i((\mathbf{k}_1-\mathbf{k}_2)\cdot\mathbf{r}-\varphi(t'))]}) \end{aligned} \quad \text{(A3)}$$

which leads to

$$I(\mathbf{r},t') = (\frac{1}{2} I_0 \, e^{[-\frac{2\mathbf{r}\cdot(\mathbf{I}-\hat{\mathbf{k}}_1\hat{\mathbf{k}}_1)\cdot\mathbf{r}}{w^2}]} + \frac{1}{2} I_0 \, e^{[-\frac{2\mathbf{r}\cdot(\mathbf{I}-\hat{\mathbf{k}}_2\hat{\mathbf{k}}_2)\cdot\mathbf{r}}{w^2}]}$$
$$+ \frac{1}{2} I_0 \, e^{[-\frac{\mathbf{r}\cdot(\mathbf{I}-\hat{\mathbf{k}}_1\hat{\mathbf{k}}_1)\cdot\mathbf{r}}{w^2}]} \; e^{[-\frac{\mathbf{r}\cdot(\mathbf{I}-\hat{\mathbf{k}}_2\hat{\mathbf{k}}_2)\cdot\mathbf{r}}{w^2}]} \; e^{[i((\mathbf{k}_1-\mathbf{k}_2)\cdot\mathbf{r}-\varphi(t'))]} \tag{A4}$$
$$+ \frac{1}{2} I_0 \, e^{[-\frac{\mathbf{r}\cdot(\mathbf{I}-\hat{\mathbf{k}}_1\hat{\mathbf{k}}_1)\cdot\mathbf{r}}{w^2}]} \; e^{[-\frac{\mathbf{r}\cdot(\mathbf{I}-\hat{\mathbf{k}}_2\hat{\mathbf{k}}_2)\cdot\mathbf{r}}{w^2}]} \; e^{[-i((\mathbf{k}_1-\mathbf{k}_2)\cdot\mathbf{r}-\varphi(t'))]}).$$

This can be worked out as:

$$I(\mathbf{r},t') = I_0 \, e^{[-\frac{2\mathbf{r}\cdot(\mathbf{I}-\frac{1}{2}(\hat{\mathbf{k}}_1\hat{\mathbf{k}}_1+\hat{\mathbf{k}}_2\hat{\mathbf{k}}_2))\cdot\mathbf{r}}{w^2}]} (\frac{1}{2} e^{[\frac{2\mathbf{r}\cdot(\frac{1}{2}(\hat{\mathbf{k}}_1\hat{\mathbf{k}}_1-\hat{\mathbf{k}}_2\hat{\mathbf{k}}_2))\cdot\mathbf{r}}{w^2}]}$$
$$+ \frac{1}{2} e^{-[\frac{2\mathbf{r}\cdot(\frac{1}{2}(\hat{\mathbf{k}}_1\hat{\mathbf{k}}_1-\hat{\mathbf{k}}_2\hat{\mathbf{k}}_2))\cdot\mathbf{r}}{w^2}]} + \frac{1}{2} e^{[i((\mathbf{k}_1-\mathbf{k}_2)\cdot\mathbf{r}-\varphi(t'))]} + \frac{1}{2} e^{[-i((\mathbf{k}_1-\mathbf{k}_2)\cdot\mathbf{r}-\varphi(t'))]})$$

(A5)

which gives:

$$I(\mathbf{r},t') = I_0 \, e^{[-\frac{2\mathbf{r}\cdot\mathbf{A}\cdot\mathbf{r}}{w^2}]} (cosh[\frac{2\mathbf{r}\cdot\mathbf{B}\cdot\mathbf{r}}{w^2}] + cos[\mathbf{k}_0 \cdot \mathbf{r} - \varphi(t')])$$

(A6)

where

$$\mathbf{A} = \mathbf{I} - \frac{1}{2}(\hat{\mathbf{k}}_1\hat{\mathbf{k}}_1 + \hat{\mathbf{k}}_2\hat{\mathbf{k}}_2) \tag{A7}$$

$$\mathbf{B} = \frac{1}{2}(\hat{\mathbf{k}}_1\hat{\mathbf{k}}_1 - \hat{\mathbf{k}}_2\hat{\mathbf{k}}_2) \tag{A8}$$

$$\mathbf{k}_0 = \mathbf{k}_1 - \mathbf{k}_2 . \tag{A9}$$

We define the position of the origin at the point of intersection of the centers of the crossed beams. At this position the sample cell is centered. The *z* direction is chosen along the bisector of $\mathbf{k}_1$ and $\mathbf{k}_2$ and

the x direction parallel to $\mathbf{k}_0$ defined in equation (A9), then $\mathbf{k_0} = k_0\hat{\mathbf{x}}$. Using this coordinate base, we can write

$$\mathbf{r}\cdot\mathbf{A}\cdot\mathbf{r} = x^2\cos^2\theta + y^2 + z^2\sin^2\theta \qquad \text{(A10)}$$

$$\mathbf{r}\cdot\mathbf{B}\cdot\mathbf{r} = -2\,x\,z\sin\theta\cos\theta\,. \qquad \text{(A11)}$$

To estimate the relative background hyperbolic cosine term we use the constraint that $|z| \le d/2$, where d is the thickness of the sample cell, typically d = 0.4 mm. Furthermore, we may assume for the exponent in equation (A6), leaving y out of consideration,

$$2\frac{x^2\cos^2\theta + z^2\sin^2\theta}{w_0^2} \le 2\frac{x^2}{w_0^2}\cos^2\theta + \frac{1}{2}\frac{d^2}{w_0^2}\sin^2\theta \le 3 \qquad \text{(A12)}$$

since otherwise the exponential in equation (A6) would have decayed to almost zero and therefore does not contribute to the intensity. With these two constrains it can be shown that the argument ϑ of the hyperbolic cosine equals

$$\vartheta = \frac{2d\sin\theta}{w_0}\left(\frac{3}{2} - \frac{d^2}{4w_0^2}\sin^2\theta\right)^{1/2}. \qquad \text{(A13)}$$

For a typical value of w_0 = 0.15 mm and θ = 2.2° the hyperbolic cosine is 1.03 which differs 3% from unity. For the largest sample cell with a thickness of d = 3 mm this approximation is not valid but this only affects the background intensity. Since we measure only the fringe pattern intensity by filtering the *ac* modulation out of the total signal, the hyperbolic cosine can be approximated by a unity value.

According to equation (A10) the exponent in equation (A6) contains the z-dependent term $2z^2\sin^2(\theta)/w_0^2$. With the mentioned typical values the z dependence of the fringe pattern intensity can be safely ignored, so that we finally get together with the hyperbolic cosine approximation

$$I(\mathbf{r},t') = I_0\, e^{\left[-\frac{2(x^2\cos^2\theta + y^2)}{w_0^2}\right]}\left(1 + \cos[k_0\,x - \varphi(t')]\right). \qquad \text{(A14)}$$

B. Proof of correctness Perrin factor $g_{\|}$ for the limit of aspect ratio equals 1

In the limit of an aspect ratio ($p = a/b$) of the ellipsoid of revolution approaching 1, the result of the Stokes-Einstein-Debye rotational diffusion coefficient $D_{\|}^{r}$ for a spherical particle should be obtained in equation (32), *i.e.* $g_{\|} \to 1$. In this appendix this will be proven. In equation (34) we found an expression for the Perrin factor $g_{\|}$ in the parallel case for rotation around the long (symmetry) axis

$$g_{\|} = \frac{2(p^2 - 1)}{3p(p - S)}. \qquad \text{B(1)}$$

For a prolate ($a > b$) ellipsoid of revolution the elliptic integral S has an analytic solution (equation (35)):

$$S_{prolate} = \frac{1}{\sqrt{p^2 - 1}} ln\,[p + \sqrt{p^2 - 1}]. \qquad \text{B(2)}$$

With $p = 1 + \varepsilon$, the limit of $p \to 1$ can be written as $p = \lim_{\varepsilon \to 0}(1 + \varepsilon)$. The analytic expression in equation B(2) for $S_{prolate}$ can be written as

$$S_{prolate} = \frac{ln\,[(1+\varepsilon) + \sqrt{(1+\varepsilon)^2 - 1}]}{\sqrt{(1+\varepsilon)^2 - 1}}. \qquad \text{B(3)}$$

By taking first order approximations in the limit of $\varepsilon \to 0$ this division is undetermined (0/0). The same is true for multiple application of the theorem of L'Hospital. To treat this problem one has to expand the nominator and denominator of equation B(3) in a power series. For the nominator one finds

$$ln\,[(1+\varepsilon) + \sqrt{(1+\varepsilon)^2 - 1}] = \sqrt{2\varepsilon} - \frac{\varepsilon^{3/2}}{6\sqrt{2}} + O[\varepsilon^{5/2}] \qquad \text{B(4)}$$

and for the denominator

$$\sqrt{(1+\varepsilon)^2-1} = \sqrt{2\varepsilon} + \frac{\varepsilon^{3/2}}{2\sqrt{2}} - O[\varepsilon^{5/2}]\,. \qquad \text{B(5)}$$

By dividing this two results, one can derive for $S_{prolate}$ in the limit of $\varepsilon \to 0$

$$\lim_{\varepsilon\to 0} S_{prolate} \sim 1 - \frac{\varepsilon}{3}\,. \qquad \text{B(6)}$$

Inserting this result in equation B(6) in the limit of $\varepsilon \to 0$ gives for the Perrin factor $g_{\|}$

$$\lim_{\varepsilon\to 0} g_{\|} = \frac{2((1+\varepsilon)^2-1)}{3(1+\varepsilon)(1+\varepsilon-1+\varepsilon/3)} = 1\,. \qquad \text{B(7)}$$

C. Correction of Perrin's paper

In his seminal paper of 1934 [24], Perrin's final expressions (his equation (95b), in this paper equation (31)) for the rotational relaxation times of the short (equatorial) axes of an ellipsoid of revolution contain a mistake [26]. Although already reported in 1943 by Wyman and Ingalls, the mistake still appeared in the classic book of Cohn and Edsall (Proteins, Amino Acids and Peptides, edition 1943 & 1965) and in several papers (for a review see [26]).

If one defines, equivalent to equations (30) and (31), the rotational relaxation times τ_0 of a sphere

$$\tau_0 \equiv \frac{1}{2D_0^r} = \frac{6\eta V_{hydro}}{2k_B T} \qquad \text{C(1)}$$

with D_0^r the rotational diffusion coefficient for a sphere, we find for the rotational relaxation time of the short axes normalized by this relaxation time for a sphere with the help of equation (31)

$$\frac{\tau_b}{\tau_0} = \frac{\tau_c}{\tau_0} = \frac{D_0^r}{D_a^r + D_c^r} = \frac{D_0^r}{D_{\parallel}^r + D_{\perp}^r} . \qquad \text{C(2)}$$

Using equations (32) and (33) for $D_{\parallel}^r$ and $D_{\perp}^r$ respectively, with the help of equation (34) for the Perrin factors $g_{\parallel}$ and $g_{\perp}$, and an aspect ratio $p=a/b$, we find after some algebraic manipulation

$$\frac{\tau_b}{\tau_0} = \frac{8}{3} \frac{p^4 - 1}{(p^2 - 2) p \, 2S + 2p^4} \qquad \text{C(3)}$$

where S is defined [27] in equation (35) for a prolate ellipsoid of revolution. The error in Perrin's paper is in the term $(p^2 - 2)$ in the denominator of equation C(3). In Perrin's notation (Perrins' equation (95b) with another definition of S ($S_{Perrin} = \frac{2S}{b}$) and eliminating p (p = a/b) , Perrin found

$$\frac{\tau_b}{\tau_0} = \frac{8}{3}\frac{a^4 - b^4}{b^2(2b^2 - a^2)a\,S_{Perrin} + 2a^4} \qquad \text{Wrong! C(4)}$$

where the sign of term in the denominator of equation C(4) multiplying S_{Perrin} is incorrect. The correct expression is:

$$\frac{\tau_b}{\tau_0} = \frac{8}{3}\frac{a^4 - b^4}{b^2(a^2 - 2b^2)a\,S_{Perrin} + 2a^4}. \qquad \text{C(5)}$$

In his equations [96] and [96bis], Perrin replaces S_{Perrin} by an analytic expression for a prolate ellipsoid of revolution, equivalent to equation (35), and an oblate ellipsoid of revolution, respectively. In these equations the expression for τ_b / τ_0 contains the same mistake.